The International Journal of Advanced Manufacturing Technology (2018) 98:2031–2055
https://doi.org/10.1007/s00170-018-2359-1

ORIGINAL ARTICLE

Experimental and analytical study of ultrasonic elliptical vibration cutting on AISI 1045 for sustainable machining of round-shaped microgroove pattern

Rendi Kurniawan[1] · S. Thirumalai Kumaran[2] · Saood Ali[1] · Dwi Ayu Nurcahyaningsih[3] · Gandjar Kiswanto[4] · Tae Jo Ko[1]

Received: 13 November 2017 / Accepted: 15 June 2018 / Published online: 28 June 2018

Abstract
This research report deals with an experimental and analytical study of the ultrasonic elliptical vibration cutting (UEVC) process on medium steel alloy (AISI 1045) for sustainable machining of round-shaped (R-shaped) microgrooves via relatively low-speed machining (0.5–2.5 m/min). The need for microgroove patterns on planar surfaces in the tribology field has increased significantly owing to superior lubrication performance in decreasing the coefficient of friction. Analyzing the surface roughness, microgroove morphology, cutting force, and chip formation during microgrooving are the main objectives of this experimental study. The experimental results showed that the UEVC process evidently produces lower surface roughness, lower cutting forces, better groove shape morphology, thinner chip thickness, and higher flow shear angle when compared to the conventional cutting process. A new approach in methods to analyze surface roughness and cutting force in UEVC microgrooving has also been developed and validated with the experimental results. Finally, these experimental studies indicate the achievement of sustainable machining of the R-shaped microgroove pattern using the UEVC process.

Keywords Elliptical vibration · Microgrooves · Surface roughness · Cutting force · Chip formation

1 Introduction

The demand for microgroove patterns has grown significantly in the tribology field, especially for controlling the friction coefficient and wear during the wet sliding contact condition [1]. In the field of tribology, the advanced geometric shapes for tribology surfaces are generally on the micrometer scale, such as grooves and dimples, which have been proven theoretically or experimentally to improve the lubrication performance [2]. The hydrodynamic pressure effect was considered as the reason for the friction reduction phenomenon [3]. Thin lubricant films are produced during sliding contact because the microgrooves behave as lubricant reservoirs that supply the lubricants into two sliding contact surfaces [4]. Consequently, owing to the hydrodynamic pressure effect, the planar surface with the microgrooves significantly increases the load carrying capacity of the lubrication fluid film [5]. Because of this tribological property, the aim of the current research is to investigate the sustainable machining of microgrooves using the UEVC process.

Owing to the tribological benefits of the microgroove patterns, the real application of the microgrooves is recently to improve the tribological performance of cutting tools during machining. The use of the microgrooves for anti-adhesion purposes on the rake face of the cutting tool has increased significantly in academia [6]. The microgrooves pattern provides a lubricant fluid on the tool chip contact zone, which is difficult to access by the lubricant fluid; consequently, the contact length between the rake face and chip reduces significantly [7]. The microgroove pattern on the rake face gives the possibility of sustainability in dry cutting operation [8]. Moreover, the benefits of the microgroove pattern on the rake

✉ Tae Jo Ko
tjko@yu.ac.kr; http://cam.ac.kr

[1] School of Mechanical Engineering, Yeungnam University, 214-1, Dae-dong, Gyeongsan-si, Gyeongsangbuk-do 712-749, South Korea

[2] Faculty of Mechanical Engineering, Kalasalingam University, Krishnankoil, Tamil Nadu 626126, India

[3] School of Materials Science and Engineering, Yeungnam University, Gyeongsan 38541, South Korea

[4] School of Mechanical Engineering, Universitas Indonesia, Kampus Baru UI, Depok 16424, Indonesia

face surface include capturing the wear debris, reducing the crater and flank wear of the tool, reducing cutting forces, and reducing the machining temperature [7]. The cutting forces reduce when the microgroove direction on the rake face of the cutting tool is perpendicular to the relative cutting speed, whereas the cutting forces remain similar or slightly larger when the microgroove direction is parallel to the cutting speed [9]. Owing to the effect of the microgroove pattern, the friction coefficient on the rake face during dry cutting assessments is smaller than that of non-nano/microgrooved cutting tools [10]. The microgrooved cutting tool significantly reduces the rake face temperature by approximately 103 °C as compared with an untextured cutting tool [11].

In 1994, Shamoto and Moriwaki [12] introduced the elliptical vibration cutting (EVC) process. Since then, the EVC process become a popular process in academia because it has excellent material removal characteristics, including the following:

- Decreasing cutting energy [13]
- Achieving mirror surface on ferrous material [14]
- Suppressing the burrs [15]
- Avoiding a premature tool breakage [16]
- Improving the tool wear rate [17]
- Cutting possibility to hard or brittle material [18]

Shamoto and Moriwaki [16] induced the EVC process for cutting of hard steel alloy (39 HRC) using a diamond tool. A lower cutting energy than the conventional cutting (CC) process was evidently obtained by the EVC process. Zhang et al. [19] experimentally explored the ultrasonic elliptical vibration cutting (UEVC) on Stavax (49 H_RC) workpiece using a polycrystalline diamond (PCD) tool. They concluded that the usage of the PCD tool in the UEVC process is suitable for fabrication of die and mold parts from the hard steel alloy [19]. Furthermore, the PCD tool wear did not appear significantly when using the UEVC process with low rotational spindle speeds of 15 and 30 rpm. Suzuki et al. [20] reported that the UEVC process significantly increases the critical depth of cutting brittle material such as sintered tungsten carbide (WC). Ma et al. [15] reported that the smallest of stress both pushing and bending the deformation zone on the workpiece edge could be realized by inducing the UEVC process, resulting in the elimination of the burrs after cutting. The EVC process reduces the damage of the diamond cutting tool after cutting distance at 2800 m when cutting of hardened die steel (JIS: SUS420J2), as reported by Shamoto and Moriwaki [16]. Nath et al. [17] suggested that the PCD tool is suitable to cut a hard and brittle material such as sintered WC when the EVC process was utilized. With increasing speed ratio of the EVC process, the cutting loads on the cutting edge increase and the tool wear growth increases; therefore, the surface finish deteriorates due to rapid tool wear [18].

Because the UEVC process is very popular, recent advanced research in UEVC between 2015 and 2017 has developed widely into specific cases, such as cutting force modeling [21], composite cutting [22], hard brittle cutting [23], mirror surface finishing [14], mechanical polishing [24], transducer development [25], suppression of frictional chatter [26], finite element modeling [27], sculpturing surface [28], micro/nanomachining [29], surface gratings [30], microdimple fabrication [31], and surface texturing [32]. Cutting force is an important machining output that correlates directly to the quality of the product such as surface integrity. Efficient cutting by means of low cutting energy is generally obtained using the UEVC process because of the effect of the elliptical trajectory of the tool; therefore, lower chip thickness and larger shear angle are obtained (Kim and Loh [13, 33]). The UEVC process significantly decreases the subsurface fracture of carbon fiber reinforced plastic (CFRP) because of a low localized stress in the interaction region between the tool tip and fiber [34]. The UEVC process realizes the ductile mode cutting in brittle materials, such as sintered WC, in which the machinability of brittle materials correlates with the grain size and binder phase [35]. Saito et al. [14] investigated the correlation between the amount of diamond wear and the composition elements of the alloy steels during mirror surface machining using the UEVC process. Their result showed that the alloy elements of tungsten and vanadium in the workpiece matrices caused rapid wear of the diamond tool because of the thermochemical interaction phenomenon [14]. The UEVC process has been adopted for mechanical polishing, in which high numerical aperture can be obtained with a ten-point mean surface roughness (R_z) up to 8 nm [36]. It has also been proven experimentally and theoretically that the chatter occurring in ordinary cutting can be suppressed significantly using the UEVC process [37], because the cutting energy of the UEVC process clearly approaches zero, and the magnitude of workpiece displacement in time domain is relatively small with the UEVC process [37]. Kurniawan et al. [32] reported that the surface roughness of micro-dimple pattern by applying the two-frequency elliptical vibration texturing process is lower than that using the conventional texturing in the low vibration frequency range. Based on the recent literatures above, the UEVC process is a promising cutting process. However, a significant number of studies related to microgrooving in medium alloy steel have been rarely reported, mostly in low-strength materials such as aluminum, copper, and brass [13, 33]. An experimental study associated with microgrooving induced by the UEVC process is reported in this paper.

Investigations of advanced microgrooving induced by the UEVC process have gained much attention in academia. Recent advanced microgrooving induced by the UEVC process shows that the majority of grooves were V-shaped, in which sharp cutting edge and V-shaped diamond tools were

used [38]. The UEVC process significantly suppresses the burrs at the exit and side region of the microgrooving and decreases the cutting energy, although the surface roughness inside the microgrooves was distorted owing to the effect of overlapped elliptical locus of the tool (Kim and Loh [13, 33]). During the microgrooving process, the UEVC process produces a smaller curvature radius and thickness of chip formation because of the effect of increasing of the shear angle and decreasing of the friction force between the chip and the tool [39]. The vibration frequency of the elliptical locus (f_m) and the cutting speed (V_f) are two main factors to determine the quality of the microgrooves. By applying a high cutting speed ratio(V_f/f_m), the vibration marks on the microgrooves were clearly observed. Otherwise, a low cutting speed ratio (V_f/f_m) decreases the surface roughness of the microgrooves and the vibration marks become difficult to observe with the naked eye [40]. A larger shear angle than that of ordinary cutting in the primary cutting zone appears as a factor in decreasing the cutting force in the UEVC process during microgrooving (Kim and Loh [13, 33]). The cutting forces during microgrooving in the UEVC process can be predicted by calculating the cross-sectional cutting area in the cutting direction to obtain the removed chip volumes per vibration cycle [41]. The microgroove geometry is essentially overlapped microdimple array at low cutting speed ratio (V_f/f_m) by the elliptical vibration texturing (EVT) process [42]. Based on the literature mentioned above, this study aims to experimentally investigate the feasibility of the UEVC process during R-shaped microgrooving.

In the UEVC process, an analytical method to predict the cutting forces in the UEVC process has been presented recently. The amount of the workpiece material that has been removed and the specific cutting pressure are associated directly with the value of the cutting forces in the UEVC process [41]. Ma et al. [43] determined the thrust cutting force in the UEVC process by applying a Fourier series. The state of the thrust cutting force was assumed to be in the normal (positive) or reversed (negative) direction as a rectangular cycle in the intermittent cutting state. The Fourier series was adopted to analyze the state of the thrust cutting force in the UEVC. It was hypothesized that the reversed thrust cutting force leads to reducing the average cutting force and the chip thickness and helps the chip to flow out [43]. Shamoto et al. [44] proposed to calculate the resultant cutting force in 3D-EVC by calculating the time instants at critical tool positions. An orthogonal cutting force analysis has been conducted by Zhang et al., in which the transient cut thickness is calculated [45]. Meanwhile, Bai et al. [21] proposed a nonequidistant shear zone model to predict the shear angle, tool-chip friction angle, and shear angle to predict the cutting force in the EVC; thus, the experiments are not necessary to conduct. Jieqiong et al. [46] proposed an analytical calculation to predict the cutting force components in the oblique EVC process. Their approach is based on calculation of the transient cut thickness and the transient shear angle. The transient shear angle is determined by using the maximum shear stress principle [46].

Although much effort has been expended in the EVC process, the research in the EVC process has not finished yet. This research report deals with the experimental and analytical study of the UEVC process on medium steel alloy (AISI 1045) for sustainable machining of round-shaped (R-shaped) microgrooves in relatively low-speed machining (0.5–2.5 m/min). The objective of this research is to extend the information in the UEVC process to establish the microgrooves pattern. The main objective of this paper is to introduce a new analytical method of surface roughness and cutting force which is based on data regression analysis.

2 Profiles of microgrooves

There are numerous profiles of microgroove patterns based on the geometry of the cutting tool. The various profiles of microgrooves as shown in Fig. 1 can be divided into four kinds of shapes: V-shaped, saw tooth, rectangular, and R-shaped grooves. In the case of V-shaped grooves, it can be further divided into three types: type I (Fig. 1a), type II (Fig. 1b), and type III (Fig. 1c). In general, the V-shaped microgrooves of type I (Fig. 1a) are symmetric V-shaped grooves and implemented for diffraction gratings [47]. The V-shaped microgrooves of type II (Fig. 1b) are symmetric V-shaped grooves with an equal distance/gap for each groove, and their functionality is usually for tribological purposes, such as friction reduction, anti-adhesion, and capturing the wear debris [47]. The V-shaped microgrooves of type III (Fig. 1c) have trapezoid shape, and their functionality is for the microchannels of micro/nanofluidic [48]. Figure 1d shows a saw tooth-shaped microgroove, which has nonsymmetrical V-shaped grooves. This saw tooth-shaped grooves are used widely in Fresnel lens applications [49]. Figure 1e shows R-shaped microgrooves, which are usually implemented for a lenticular lens mold [50]. The wire-electrical discharge machining plus electrolytic polishing is capable to manufacture precisely the lenticular pattern mold; however, its slow machining rate (30–10 μm/s) is a major disadvantage of this process [51]. In the case of rectangular microgroove (Fig. 1f), the rectangular-shaped microgrooves need a special rectangular cutting tool to manufacture that kind of shape. The suitable method to fabricate the rectangular shaped microgroove is by using the electrical discharge machining [52]. The rectangular shape is easily made by using micromilling method; nevertheless, because

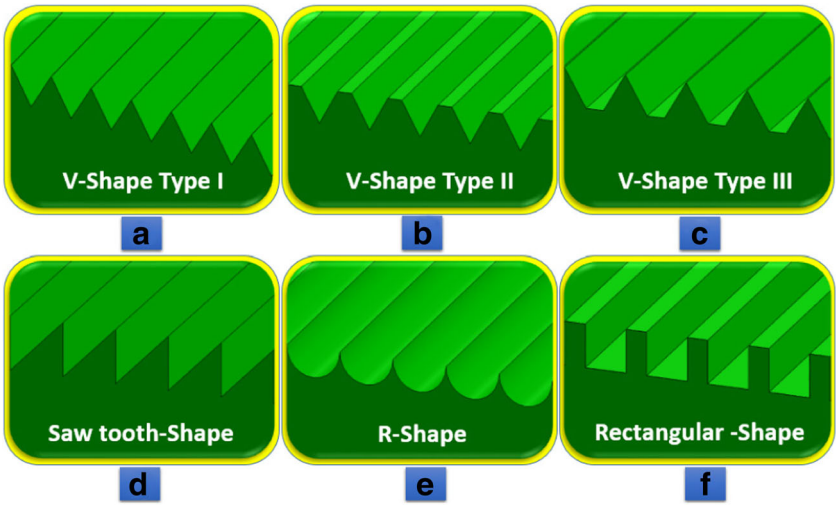

Fig. 1 General variations of microgroove shape. **a** V-shape type I. **b** V-shape type II. **c** V-shape type III. **d** Saw tooth-shape. **e** R-shape. **f** Rectangular (Sawada et al. 2000)

significant burrs appears during microgrooving/slotting process, the micromilling process must be optimized [53].

In the case of R-shaped microgroove, there are two kinds of microgrooving. Figure 2 shows the round-shaped tool tip cut along the cutting speed direction with the gap between two neighbored grooves is greater than zero (Fig. 2a) and for equal to zero (Fig. 2b). Because the cutting tool edge has a round shape, the shape of the microgroove replicates the shape of the cutting tool. The microgrooves pattern with Lb is greater than zero as main objective in this paper. The R-shaped

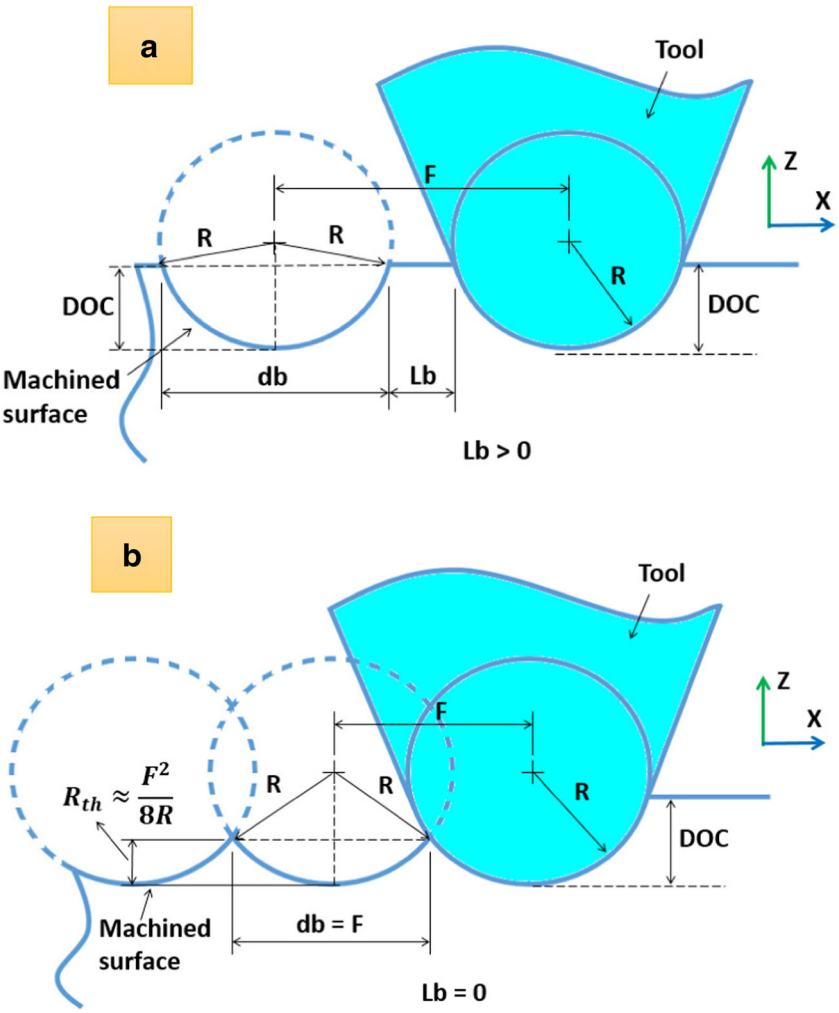

Fig. 2 Two types of R-shaped microgrooving. **a** Lb > 0. **b** Lb = 0

microgrooves of width (*db*) as shown in Fig. 2 can be determined as follows:

– If the gap between two neighbored grooves (Lb) > 0

$$db = 2\sqrt{R^2-(R-DOC)^2} \tag{1}$$

– If the gap between two neighbored grooves (Lb) = 0

$$db = F \approx 2\sqrt{R^2-\left(R-\frac{F^2}{8R}\right)^2} \tag{2}$$

3 EVC principle

Figure 3 illustrates the cutting tool vibrating sequentially in two dimensions in the Cartesian coordinate (*y*-*z*) plane. The *y*-axis is for cutting direction, and the *z*-axis is for depth of cut (*DOC*) direction. The neutral axis represents when the cutting tool does not vibrate; in other words, the CC process takes place. In general, the cutting tool vibrates sequentially in two directions by the piezo actuators to establish an elliptical locus [54]. The elliptical locus overlaps in each period when the maximum cutting tool vibration speed is higher than the nominal cutting speed in the *y*-direction ($2\pi f_m a > V_F$). ($2\pi f_m a > V_F$) is the requirement for intermittent cutting in the EVC process. The cusp of the machined surface is formed when the elliptical locus overlaps in each period. The cutting tool begins to cut at point A (see Fig. 3) and establishes the cusp of machined surface at point A. In the EVC process, *DOC* changes periodically in each period, namely the transient thickness of cut (TOC_t) [45]. At point B, the maximum TOC_t occurs, which means the load on the rake face of the cutting tool is maximum. The cutting tool begins to climb at point C and the shear angle value remains inconstant namely transient shear angle [45] when the slope angle $\theta(t)$ is larger than the shear angle during the CC process. The friction reversal effect occurs when the cutting tool reaches from point C to point D. The cutting tool disengages the deformed chip at point D and the EVC process finishes during one period. The friction reversal effect is considered by many scientists as causing the decreased cutting forces [45].

Assuming the cutting tool vibrates sequentially in the *y*- and *z*-directions, the relative motion of the cutting tool with respect to the stationary workpiece can be expressed as follows:

$$y(t) = a\cdot\cos(2\pi f_m\cdot t) + a - V_F\cdot t \tag{3}$$

$$z(t) = b\cdot cos(2\pi f_m\cdot t + \phi) + b \tag{4}$$

The *y*-axis and *z*-axis amplitude is expressed by *a* and *b*, respectively. f_m is the ultrasonic vibration frequency, V_F is the relative cutting speed in the *y*-direction, ϕ is the phase shift which was set at constant 90° in this study, and *t* is the time.

The cutting tool velocity relative to the workpiece can be derived as the time-derivative of the cutting tool position, in the *y*-axis and *z*-axis directions:

$$V_y(t) = \frac{dy(t)}{dt} = -2\pi f_m\cdot a\cdot\sin(2\pi f_m\cdot t) - V_F \tag{5}$$

$$V_z(t) = \frac{dz(t)}{dt} = -2\pi f_m\cdot b\cdot\sin(2\pi f_m\cdot t + \phi) \tag{6}$$

where $V_y(t)$ and $V_z(t)$ are the cutting tool velocity in the *y*- and *z*-directions, respectively. The transient velocity vector and the magnitude velocity are described in Eqs. 7 and 8, respectively:

$$\overrightarrow{V_t}(t) = V_y(t)\,\vec{j} + V_z(t)\,\overrightarrow{k} \tag{7}$$

$$|V_t(t)| = \sqrt{V_y(t)^2 + V_z(t)^2} \tag{8}$$

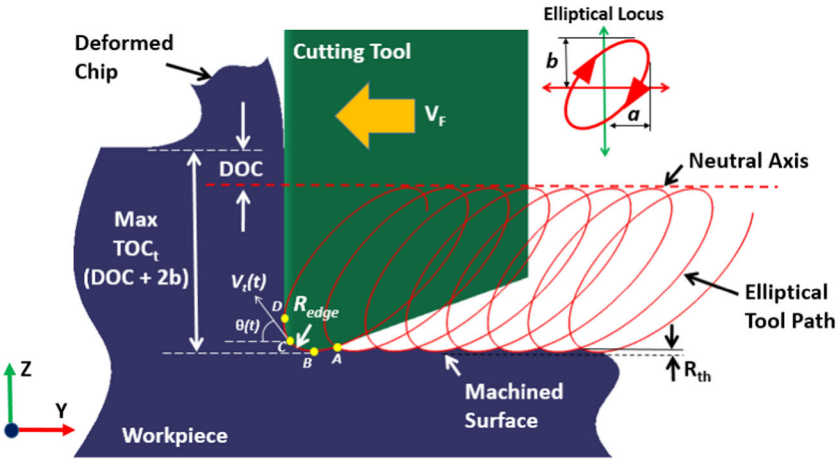

Fig. 3 Illustration of the EVC process

The slope angle of the elliptical path $\theta(t)$ is defined relative to the y-axis, and it can be described as follows:

$$\theta(t) = tan^{-1}\left(\frac{V_z(t)}{V_y(t)}\right) = tan^{-1}\left(\frac{-2\pi f_m \cdot b \cdot \sin(2\pi f_m \cdot t + \phi)}{-2\pi f_m \cdot a \cdot \sin(2\pi f_m \cdot t) - V_F}\right) \quad (9)$$

3.1 Surface roughness model

In this study, the surface roughness that is generated by the EVC process is modeled and consists of two components. The first component is theoretical roughness in which the cutting edge radius is considered [32, 55], and the second component is a residual error, which is modeled using a regression analysis. Equation 10 describes the surface roughness model used to predict the generated surface roughness by the EVC process. R_{e_th} is the theoretical surface roughness, and R_{res} is the residual error surface roughness.

$$R_{evc} = R_{e\_th} + R_{res} \quad (10)$$

The theoretical surface roughness is modeled by considering the kinematic of the cutting tool and the effect of the cutting edge radius which was proposed by Zhang et al. [55]. Figure 4 shows the illustration of the machined surface in the EVC process by considering the effect of the cutting edge radius. A typical machined surface with vibration marks observed by atomic force microscope and scanning electron microscopy is shown in Fig. 7a when a small cutting edge radius such as a single crystal diamond tool was utilized. The cutting edge was assumed that has a circular shape and the cutting edge radius is R_e. The point **CL** represents the cutter location and the point **CC** represents the cutter contact, in which the effect of the cutting edge radius is not considered. The point **CC'** is new cutter contact location at which the effect of cutting edge radius is considered [32].

Point **CC'** is located at the red colored surface profile, as shown in Fig. 4. The coordinate of point **CC'** can be determined as follows [32, 55]:

$$y_e(t) = a \cdot \cos(2\pi f_m \cdot t) + a - V_F \cdot t - R_e \cdot sin\theta(t) \quad (11)$$

$$z_e(t) = b \cdot \cos(2\pi f_m \cdot t + \phi) + b + R_e \cdot (1 - \cos\theta(t)) \quad (12)$$

where $\theta(t)$ is the slope angle of the elliptical path, and $sin\theta(t)$ and $cos\theta(t)$ are determined using the following equations [55]:

$$sin\theta(t) = \frac{V_z(t)}{\sqrt{V_y(t)^2 + V_z(t)^2}} \quad (13)$$

$$cos\theta(t) = \frac{-V_y(t)}{\sqrt{V_y(t)^2 + V_z(t)^2}} \quad (14)$$

where $V_y(t)$ and $V_z(t)$ are the cutting tool velocity in the y- and z-directions, as obtained from Eqs. 5 and 6, respectively. Figure 5 shows that the $\theta(t)$ is measured from the horizontal line with respect to the velocity vector $V_t(t)$.

To determine the theoretical surface roughness R_{e_th}, the new cusp point **Cp'**(y_e,z_e) must be found using the Newton–Raphson numerical method. Point **Cp'**(y_e,z_e) is indicated by a blue dot (Fig. 5). R_{e_th} is determined from point **Cp'**(y_e,z_e) to the zero reference $(z_e(t) = 0)$, as shown in Fig. 4. Thus, R_{e_th} equals $z_e(t_A)$ or $z_e(t_A')$ at certain time t_A and t_A', where t_A is a time when the cutting tool leaves the profile, and t_A' is a time when the cutting tool comes in the profile in one period (see Fig. 5); thus, the theoretical surface roughness R_{e_th} is described as follows [55]:

$$R_{e\_th} = z_e(t_A) = b \cdot cos(2\pi f_m \cdot t_A + \phi) + b + R_e \cdot (1 - cos\theta(t_A)) \quad (15)$$

or,

$$R_{e\_th} = z_e\left(t_A'\right) = b \cdot cos\left(2\pi f_m \cdot t_A' + \phi\right) + b + R_e \cdot \left(1 - cos\theta\left(t_A'\right)\right) \quad (16)$$

The horizontal distance between the y-axis coordinates of the two cusp points **Cp'**$(y_e(t_A),z_e(t_A))$ and **Cp'**$(y_e(t_A'),z_e(t_A'))$ is

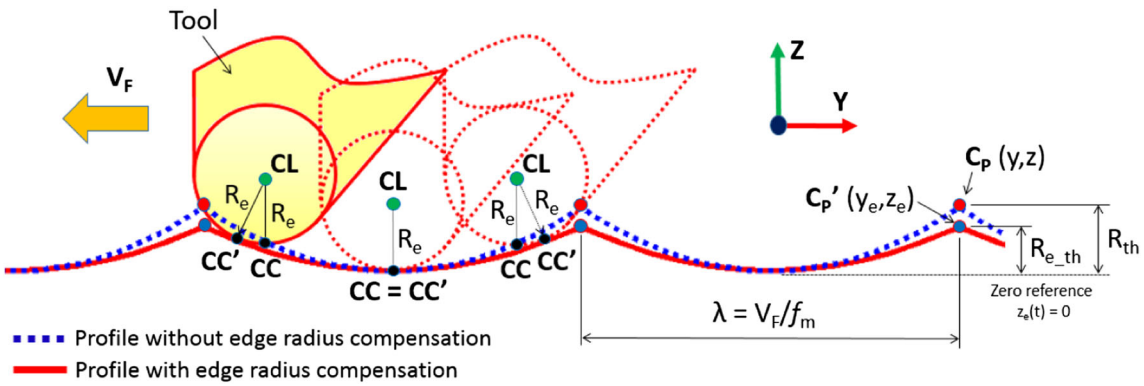

Fig. 4 Illustration of the machined surface in the EVC process adopted from Zhang et al. (Zhang et al. 2013)

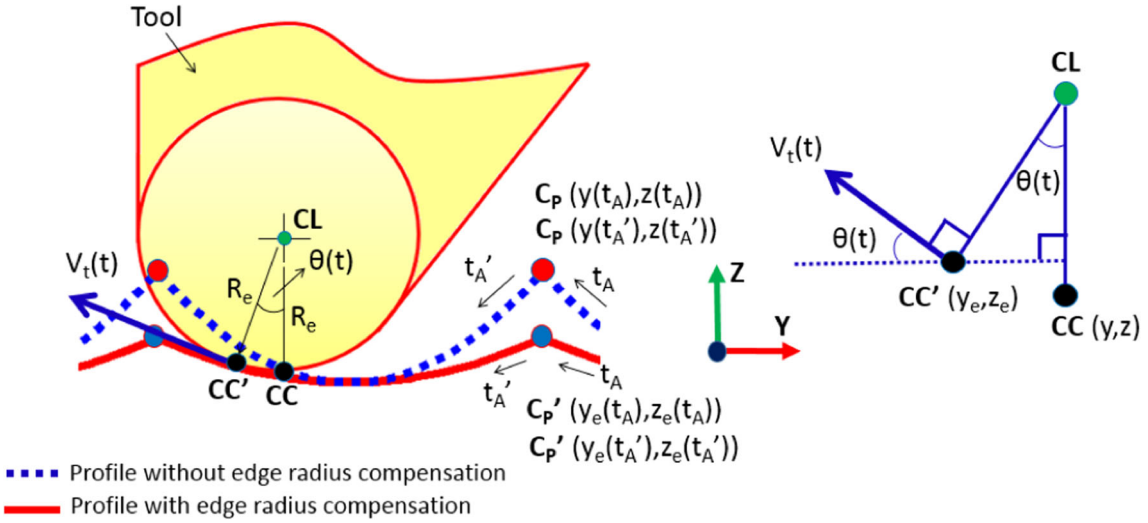

Fig. 5 Enlarged view to determine point CC'

equal zero, and the vertical distance in the z-axis coordinate between two cusp points is also equal zero; thus, the following equation can be used to determined t_A and t_A' by using the Newton–Raphson method [32]:

$$\begin{cases} y_e(t_A) - y_e\left(t_A'\right) = 0 \\ z_e(t_A) - z_e\left(t_A'\right) = 0 \end{cases} \tag{17}$$

Figure 6a shows the effect of the cutting edge radius that is varied from 0 to 3 μm, and the cusp of the surface profile reduces when the R_e increases from 0 to 3 μm. Figure 6b shows the relationship between R_{e_th} and R_e in various nominal cutting speeds V_F: with increasing R_e, R_{e_th} decreases significantly. In addition, the nominal cutting speed also influences the theoretical surface roughness. It can be understood that with increasing nominal cutting speeds, R_{e_th} increases.

The residual surface roughness R_{res} is added in the EVC roughness model. Because the theoretical surface roughness R_{e_th} is not sufficient to predict the roughness, especially at low speed ratio [32]. There is a large difference between R_{e_th} and the arithmetic measured value R_a. The second-order regression analysis was adopted to develop the model of R_{res}. The R_{res} value is obtained using Eq. 18, and the general model of regression analysis of R_{res} is presented in Eq. 19 as a function of the cutting speed V_F and the depth of cut DOC.

$$R_{res} = R_a - R_{e\_th} \tag{18}$$

$$R_{res} = C_0 + C_1 \cdot V_F + C_2 \cdot DOC + C_{11} \cdot {V_F}^2 + C_{22} \cdot DOC^2 + C_{12} \cdot V_F \cdot DOC \tag{19}$$

where C_o represents a constant coefficient, C_1 and C_2 represent linear constant coefficients, C_{11} and C_{22} represent quadratic constant coefficients, and C_{12} represents an

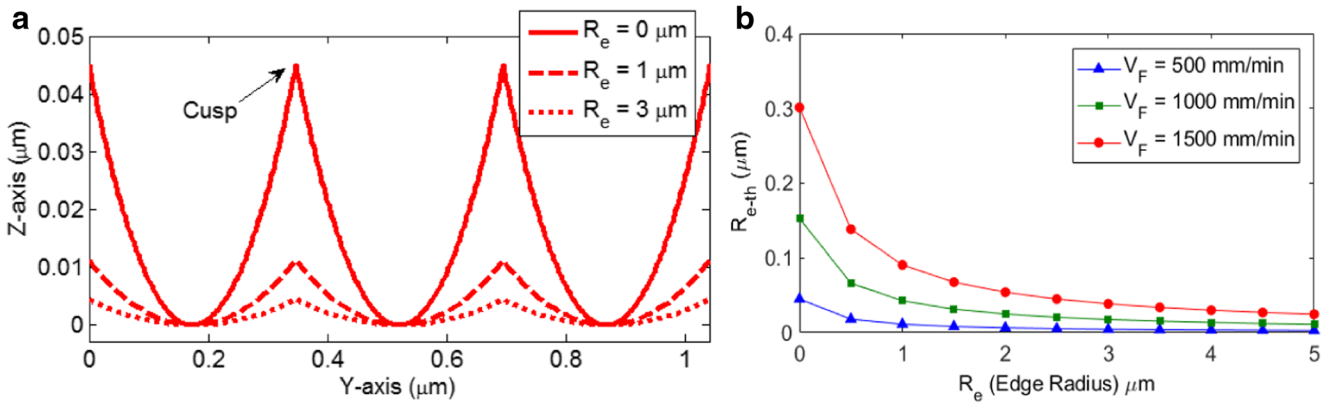

Fig. 6 **a** Simulation of surface profiles along the y-axis direction considering tool edge radius at $V_F = 500$ mm/min. **b** R_{e_th} versus the cutting edge radius R_e in various cutting speeds

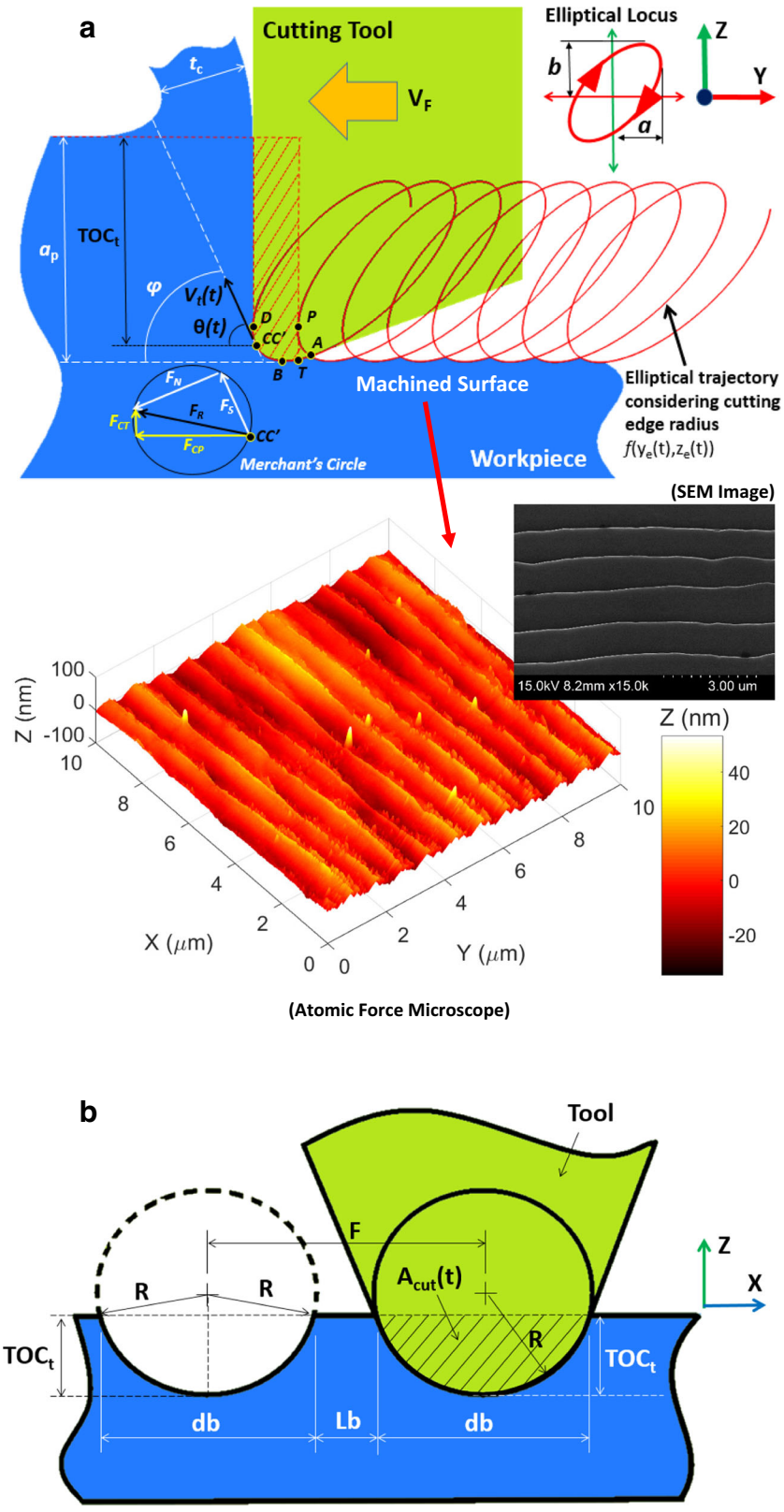

Fig. 7 Illustration of microgrooving in the EVC process. **a** Transient thickness of cut $TOC_t(t)$. **b** Area of cut $A_{cut}(t)$

interaction constant coefficient. By using Eq. 19, the roughness error can be compensated, in which the effect of *DOC* and cutting speed are considered in this microgrooving case. Based on Eq. 18, the residual surface roughness can be found and the predicted model of the R_{res} can be described empirically in Eq. 20, where V_F is in

Table 1 Definition of the time in the EVC

t	Transient time at the cutter contact point CC' lied from point A to D
t_P	Transient time in previous cycle at between point A and point P, point P is the end of cutting in previous cycle.
t_A	Time in beginning of cut at point A (at cusp point C_P')
t_T	Time when similar y_e-coordinate with point P
t_B	Time when the cutting tool passes the bottom point B
t_D	Time when the cutting tool disengages the workpiece at point D (end of cutting)

meters per minute and *DOC* is in micrometers. The flowchart diagram of the surface roughness model is shown in the Fig. 9a.

$$R_{res} = 60.2 - 24.7 \cdot V_F + 4.21 \cdot DOC - 2.26 \cdot {V_F}^2 - 0.0338 \cdot DOC^2 - 0.364 \cdot V_F \cdot DOC \quad (20)$$

3.2 Cutting force model

In this study, the cutting force model of the EVC process is inspired from Zhang's work [45]. Fundamentally, the cutting force can be determined based on how much workpiece material is removed during cutting. In the EVC case, the thickness of cut (TOC) is varied during engaging the workpiece, as illustrated in the red area in Fig. 7a. The red area illustrates that the workpiece material will be removed in one cycle period of cutting. According to the Merchant's analytical model in the orthogonal cutting [56], the principle cutting force F_{CP} and thrust cutting force F_{CT} can be expressed as follows:

$$F_{CP}(t) = \left[\frac{\tau_s \cdot \cos(\beta - \alpha)}{sin\varphi \cdot \cos(\varphi + \beta - \alpha)}\right] \cdot A_{cut}(t) \quad (21)$$

$$F_{CT}(t) = \left[\frac{\tau_s \cdot \sin(\beta - \alpha)}{sin\varphi \cdot \cos(\varphi + \beta - \alpha)}\right] \cdot A_{cut}(t) \quad (22)$$

where τ_s is shear stress on the shear plane, β is friction angle, α is rake angle, ϕ is shear angle, $A_{cut}(t)$ is transient cutting area on the rake face that is a segment of a circle as shown in Fig. 7b.

In this study, τ_s and ϕ are assumed to be constant. Thus, the cutting force coefficient for principle K_{fp} and thrust K_{ft} can be introduced for simplicity in Eqs. 23 and 24, respectively [57]. The cutting force coefficient can be found by conducting an experiment on the EVC process. The cutting force coefficient is related to the material properties, tool geometry, and machining condition.

$$K_{fp} = \frac{\tau_s \cdot \cos(\beta - \alpha)}{sin\varphi \cdot \cos(\varphi + \beta - \alpha)} \quad (23)$$

$$K_{ft} = \frac{\tau_s \cdot \sin(\beta - \alpha)}{sin\varphi \cdot \cos(\varphi + \beta - \alpha)} \quad (24)$$

Thus, Eq. 21 and Eq. 22 become

$$F_{CP}(t) = K_{fp} \cdot A_{cut}(t) \quad (25)$$

$$F_{CT}(t) = K_{ft} \cdot A_{cut}(t) \quad (26)$$

The transient cutting area $A_{cut}(t)$ is defined by Eq. 27 [31].

$$A_{cut}(t) = \left\{R^2 \cdot cos^{-1}\left(\frac{R - TOC_t(t)}{R}\right)\right\} - \left\{(R - TOC_t(t))\sqrt{2 \cdot R \cdot TOC_t(t) - TOC_t(t)^2}\right\} \quad (27)$$

where $TOC_t(t)$ is transient TOC during cutting in the red area as illustrated in Fig. 7a, and R is tool nose radius which is illustrated in Fig. 7b. $TOC_t(t)$ can be defined based on the geometrical relationships as shown in Fig. 7a. $TOC_t(t)$ at different locations from point A to point D can be defined as follows:

$$TOC_t(t) = \begin{cases} 0 & t < t_A \ , \ t \geq t_D \\ z_e(t_P) - z_e(t) & t_A \leq t < t_T \\ a_p - z_e(t) & t_T \leq t < t_D \end{cases} \quad (28)$$

where t_A, t_T, t_B, t, and t_D are time when the cutting tool passes points A, T, B, CC', and D, respectively. Table 1 defines the times of each point.

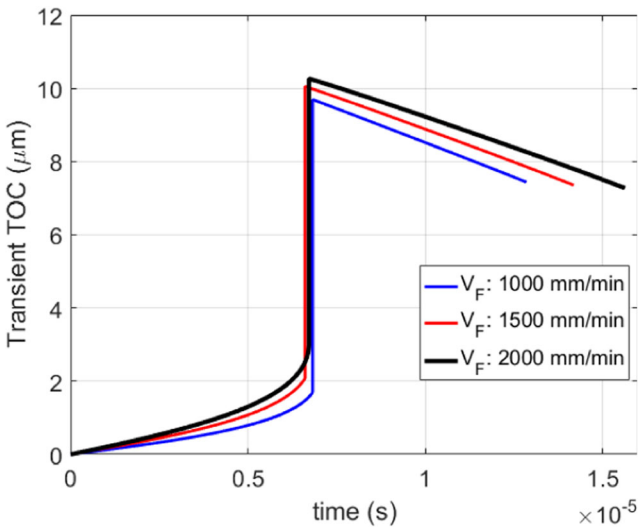

Fig. 8 Transient TOC during one duty cycle of single cutting with different nominal cutting speed V_F 1000 mm/min, V_F 1500 mm/min, and V_F 2000 mm/min

Fig. 9 Flowchart of surface roughness and cutting force model in the UEVC

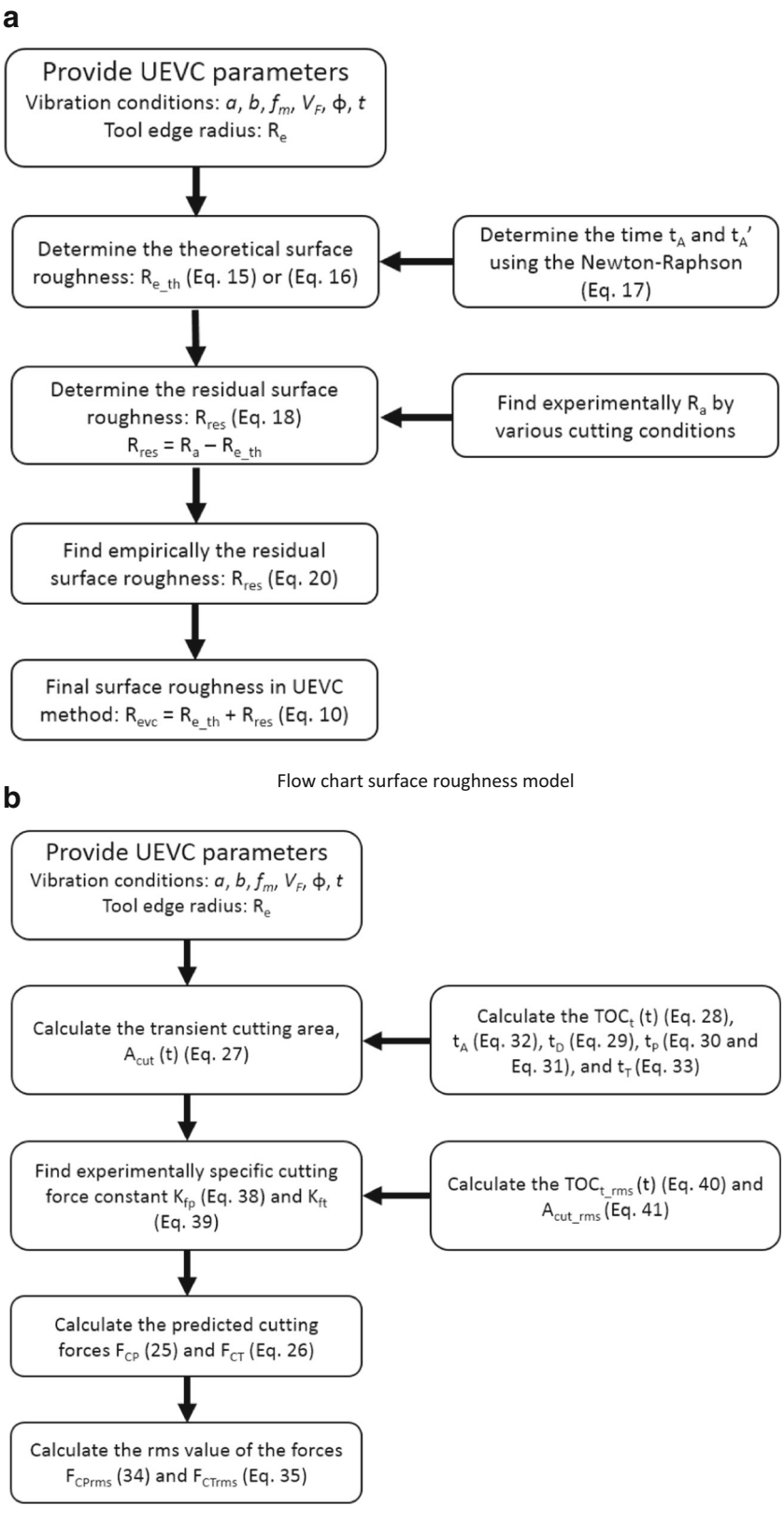

Table 2 Typical chemical compositions of AISI 1045 (wt.%) (Gao et al. 2016; Ma et al. 2016)

Material	C	Mn	Si	Cr	Ni	Al	Fe
AISI 1045	0.42–0.50	0.5–0.80	0.17–0.37	≤0.25	≤0.25	≤0.2	Balanced

The time at the end of cutting t_D can be found by numerically solving Eq. 29, because the relative speed of the cutting tool in the normal direction to the rake face goes to zero at t_D.

$$V_{ye}(t_D) = -a{\cdot}2\pi f_m{\cdot}sin(2\pi f_m{\cdot}t_D) - V_F - R_e{\cdot}\frac{d}{dt}sin\theta(t_D) = 0 \quad (29)$$

After finding t_D, t_P at point P can be easily found:

$$t_P = t_D - \frac{1}{f_m} \quad (30)$$

To determine the transient time t_P the for which the cutter lays from point A and P, a numerical approach is used to solve Eq. 31 [45]. In this study, the rake angle is equal as zero, tan $(\alpha) = 0$.

$$\frac{y_e(t) - y_e(t_P)}{z_e(t) - z_e(t_P)} = \tan(\alpha) \qquad 0 < (t - t_P) < \frac{1}{f_m} \quad (31)$$

Meanwhile, to find the time of beginning of cut t_A, the relationship in Eq. 17 can be used and a numerical method is applied.

$$\begin{aligned} y_e(t_A) - y_e\left(t_A{}'\right) &= 0 \\ z_e(t_A) - z_e\left(t_A{}'\right) &= 0 \end{aligned} \quad (32)$$

t_T can be found by finding the relationship between points P and T. Because t_P at point P has been found by Eq. 30, t_T can be found numerically by the following relationship.

$$y_e(t_T) - y_e(t_P) = 0 \qquad t_A \le t_T \le t_D \quad (33)$$

The cutting force varies during a single cutting period of time $t_{cut} = t_D - t_A$; thus, the transient cutting force is calculated as an effective cutting force by taking the root mean square (rms) value [58], where n is the number of data used in the numerical calculation from time t_A to t_D.

$$F_{CP_{rms}} = \sqrt{\frac{1}{t_{cut}}\int_{t_A}^{t_D}[F_{CP}(t)]^2 dt} = \sqrt{\frac{1}{n}\sum_{i=1}^{i=n}[F_{CP}(t_i)]^2} \quad 1 \le i \le n \quad (34)$$

$$F_{CT_{rms}} = \sqrt{\frac{1}{t_{cut}}\int_{t_A}^{t_D}[F_{CT}(t)]^2 dt} = \sqrt{\frac{1}{N}\sum_{i=1}^{i=n}[F_{CT}(t_i)]^2} \quad 1 \le i \le n \quad (35)$$

Figure 8 shows the transient TOC during each duty cycle of cutting. The simulated transient TOC increases gradually and reaches a maximum at a certain point and then decreases until the cutting tool disengages the cutting zone. $f_m = 24{,}000$ kHz, $\phi = 90°$, $a = 0.4$ μm, $b = 0.6$ μm, $R_e = 3$ μm, and $DOC = 10$ μm were used in the simulated transient TOC, as shown in Fig. 8. As we can see, with increasing nominal cutting speed V_F, the transient TOC increases owing to the effect of the elliptical trajectory, and thus, more material is cut. The flowchart diagram of the cutting force model is shown in the Fig. 9b.

4 Experimental setup

4.1 Microstructure of workpiece material

The workpiece material is a square block of the medium steel alloy AISI 1045 that has dimensions of length 20 mm, width 20 mm, and depth 20 mm. The medium steel alloy of AISI 1045 has been manufactured broadly in mechanical components such as gears, shafts, axles, crankshafts, pins, rods, bolts, pinions, forgings, bulldozer edges, machine parts, and so on [59]. AISI 1045 is considered as having good machinability, especially in turning or milling operations. In this study, AISI 1045 was produced typically from the factory with the normalized processes. In general, AISI 1045 has chemical compositions as shown in Table 2. Table 3 presents the mechanical properties of the AISI 1045 carbon steel.

In order to investigate the microstructure of the AISI 1045 surface, the metallography analysis has been evaluated through both optical microscopy and scanning electron microscopy (SEM). In order to reveal the microstructure of AISI 1045 surface before machining, the AISI 1045 surface was polished to a fine mirror finish and then chemically etched with 3% nital. After etching, the samples were evaluated. Figure 10a shows the optical microscopy of microstructure of AISI 1045 before and after 3% chemical nital etching. Before etching or after mirror polishing, the surface of AISI 1045 reveals many voids/holes (approximately 5–10 μm). The voids are indicated by the black color in Fig. 10a. The

Table 3 Mechanical properties of the AISI 1045 carbon steel (Ma et al. 2016)

Material	Density	Tensile strength, σ_u	Elastic modulus	Elongation percentage	Hardness
AISI 1045	7870 kg/m^3	917 MPa	210 GPa	15%	275 $HV_{0.5}$

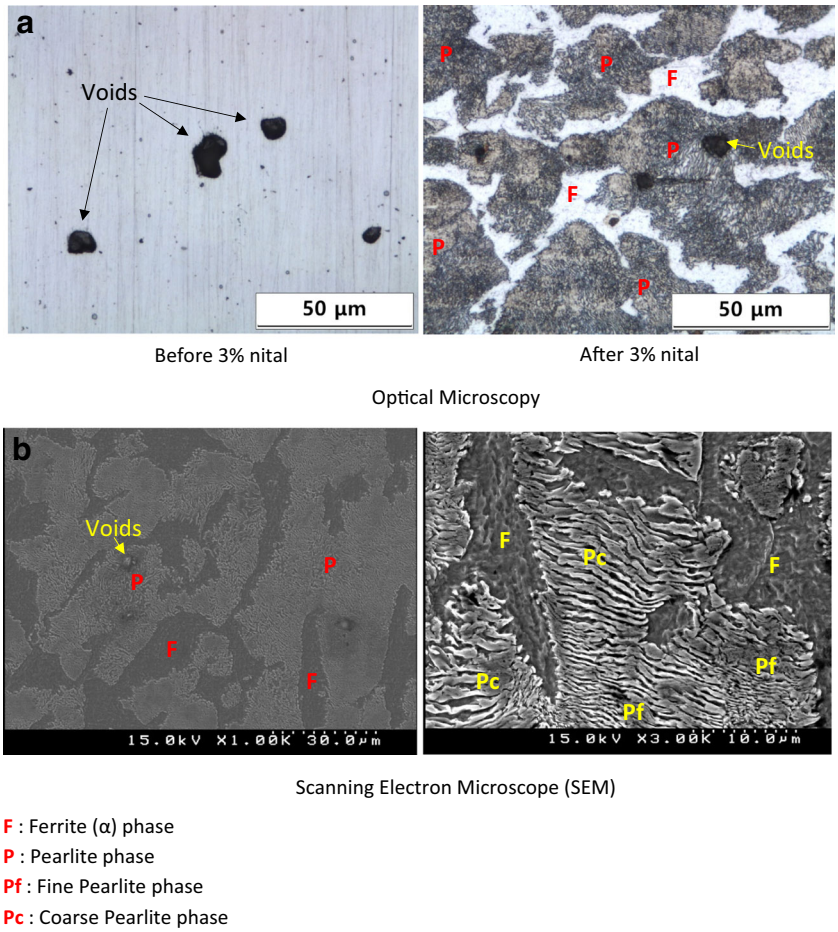

Fig. 10 Microstructure of AISI 1045. **a** Optical microscopy. **b** Scanning electron microscope (SEM)

voids might be formed owing to imperfection in manufacturing process of the AISI 1045. After etching, the optical microscopy images reveal the microstructure of the AISI 1045 that consist of the ferrite (α) phase (white color in the image) and the pearlite phase (darker color in the image), called the ferrite–pearlite formation, as shown in Fig. 10a. In the case of SEM images Fig. 10b, the ferrite (α) phase is shown by the darker color, whereas the pearlite phase is shown by the brighter color. The symbols in the images are F for the ferrite (α) phase and P for the pearlite phase. The ferrite (α) matrix uniformly surrounds the pearlite matrix boundaries. In this case, the AISI 1045 microstructure consists of approximately 70% pearlite and 30% ferrite matrixes. The ferrite (α) phase is a common component in steels and has a body-centered cubic (BCC) structure formed of iron, and in some cases, the ferrite (α) matrix tends to be more brittle and forms inclusions if manganese and silicon are involved in the ferrite (α) solution [60]. The ferrite (α) is considered as a stable matrix. The pure pearlite matrix consists of iron carbide ($Fe_3C = \overline{C}$)/cementite and the ferrite (α) matrix. The formation of thin or thick ferrite–pearlite is generally formed by a slow cooling treatment of the steels [59]. Meanwhile, a rapid/fast cooling treatment of the steels create a martensite phase, which is an extremely hard and brittle structure with poor machinability [60], although the martensite phase does not appear in this microstructure analysis. The pearlite phase is divided to two types: the coarse pearlite (Pc) and the fine pearlite (Pf), as shown in Fig. 10b. The coarse pearlite (Pc) has a coarser spacing of the platelets, and it is a relatively soft structure with good machinability [60], whereas the fine pearlite (Pf) has a finer spacing of the platelets and it typically has higher hardness and strength than the coarse pearlite (Pc) [60].

Table 4 EVC microgrooving parameters

EVC parameters	Value (unit)
Cutting speed, V_F	500–2500 mm/min
DOC	15–25 µm
Cross feed distance, F	300 µm
Vibration frequency, f_m	24 kHz
Phase shift, ϕ	90°
Minor amplitude, a	0.4 µm
Major amplitude, b	0.6 µm
Tool edge radius, R_e	3 µm

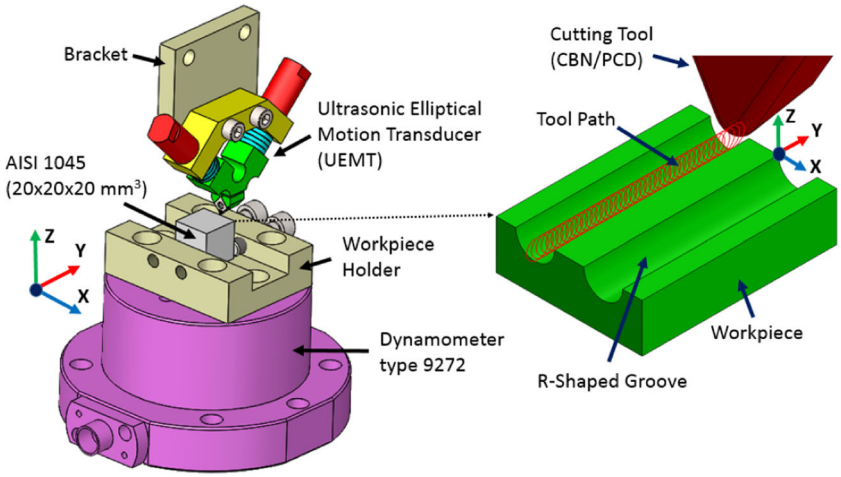

Fig. 11 The EVC experimental setup of microgrooving

4.2 Experimental procedure

The microgroove pattern was successfully manufactured on the AISI 1045 surface with the cutting parameters in Table 4. The cutting speeds were varied between 500 and 2500 mm/min. The DOC was varied from 15 to 25 µm. The cross-feed distance between two grooves was maintained as constant at 300 µm. The ultrasonic frequency was 24 kHz with a constant phase shift of 90°. In order to reduce the flatness error due to clamping the workpiece on the jig, a facing process using an end-mill tool (DIA 10 mm) was carried out first with the feed rate of 10 mm/min and the rotational spindle speed of 10,000 rpm. Then, the microgrooving processes were carried out. The workpiece material ($20 \times 20 \times 20$ mm^3) is AISI 1045,

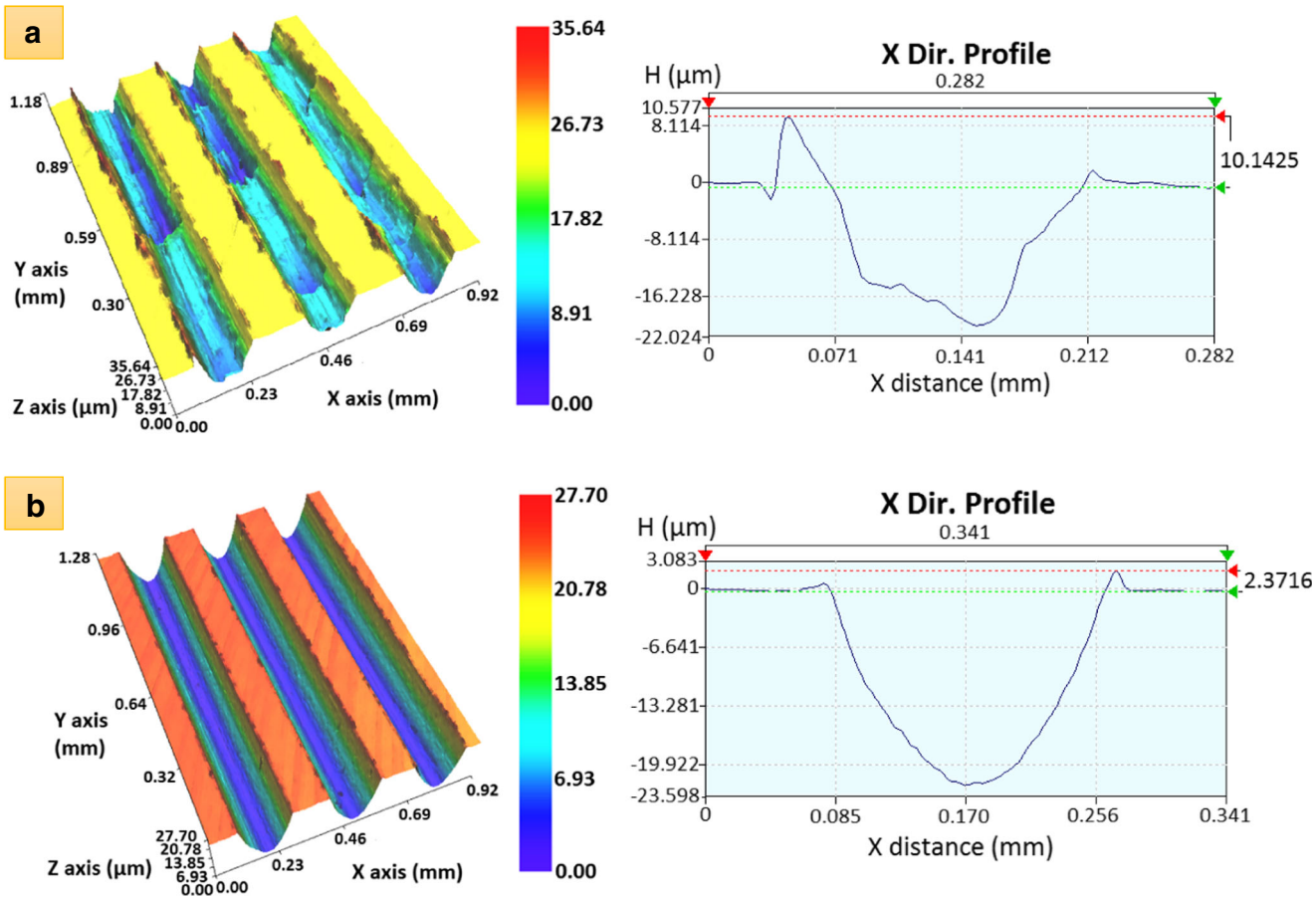

Fig. 12 Comparison 3D microgrooves surface profile between **a** CC and **b** UEVC method at V_F 1000 mm/min, DOC 20 µm, f_m 24 kHz, and ϕ 90°

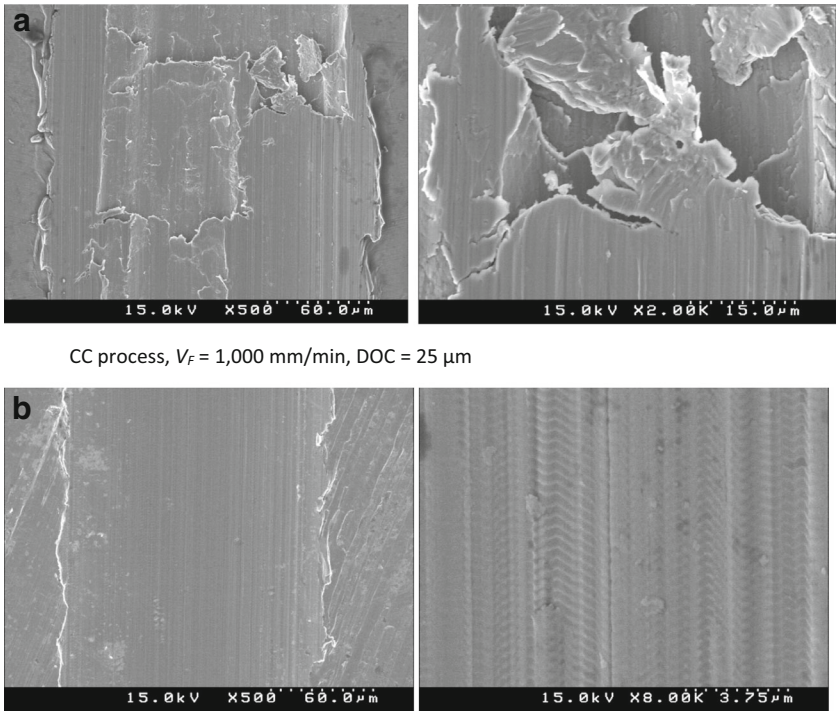

Fig. 13 SEM images between **a** the CC process and **b** the UEVC process

which is considered to have a good machinability and high strength properties, although cracks were found in some locations of the machined surface, the reasons for which are discussed in the Section 5. The cubic boron nitride (CBN) CCGW 060202 insert was used, which was manufactured by TaeguTec. In order to generate an ultrasonic elliptical motion of the tool tip, an ultrasonic elliptical motion transducer (UEMT) was used, the detail design of the which was presented previously [61]. The design of the UEMT device was inspired by Guo's design [54].

Figure 11 shows the illustration of the microgrooving experimental setup. The microgrooving process was carried out in a three-axis milling machine. As shown in Fig. 11, the spindle was removed and replaced with the UEMT device, which was attached on the bracket. The bracket and the workpiece holder (jig) were made from acrylic to avoid the potential difference between the high-voltage piezo actuator amplifier and the dynamometer while measuring the cutting forces. The piezo actuator was vibrated sequentially by the high voltage amplifier with a maximum voltage capability 400 $V_{p\text{-}p}$. A fixed voltage of 300 $V_{p\text{-}p}$ was utilized during the microgrooving experiments. A data acquisition system (National Instruments) was used to record the dynamometer signal with a sampling frequency of 40 kHz. To evaluate the surface roughness of the machined microgrooves, a 3D optical surface profiler (Nano System NV-2000) was used in which the white light scanning interferometry principle was employed. The surface morphology was also observed by SEM.

5 Experimental results and discussions

5.1 Microgrooves morphology

The microgroove pattern morphology was observed by varying the nominal cutting speeds along the y-axis direction from 500 to 2500 mm/min, and the nominal DOC was also varied from 15 to 25 µm, as shown in the microgrooving parameters in Table 4. Figure 12 shows a comparison of the 3D microgroove surface profile between the CC and UEVC method at V_F 1000 mm/min, DOC 20 µm, f_m 24 kHz, and ϕ 90°. It can be seen that the microgroove pattern using the UEVC process is evidently better than that of the CC process. Shaw [60] mentioned that a good surface morphology is very difficult to obtain in steel cutting when the relative cutting speeds are very low, i.e., lower than approximately 120,000 mm/min. The poor microgroove morphology in the CC process is typically obtained in low cutting speeds ($V_F \leq 2500$ mm/min) in these experimental studies. In contrast, the microgroove morphology in the UEVC process is typically better because as the cutting process becomes intermittent, at low cutting energy, the cutting speed relatively increases by applying the elliptical vibration [12].

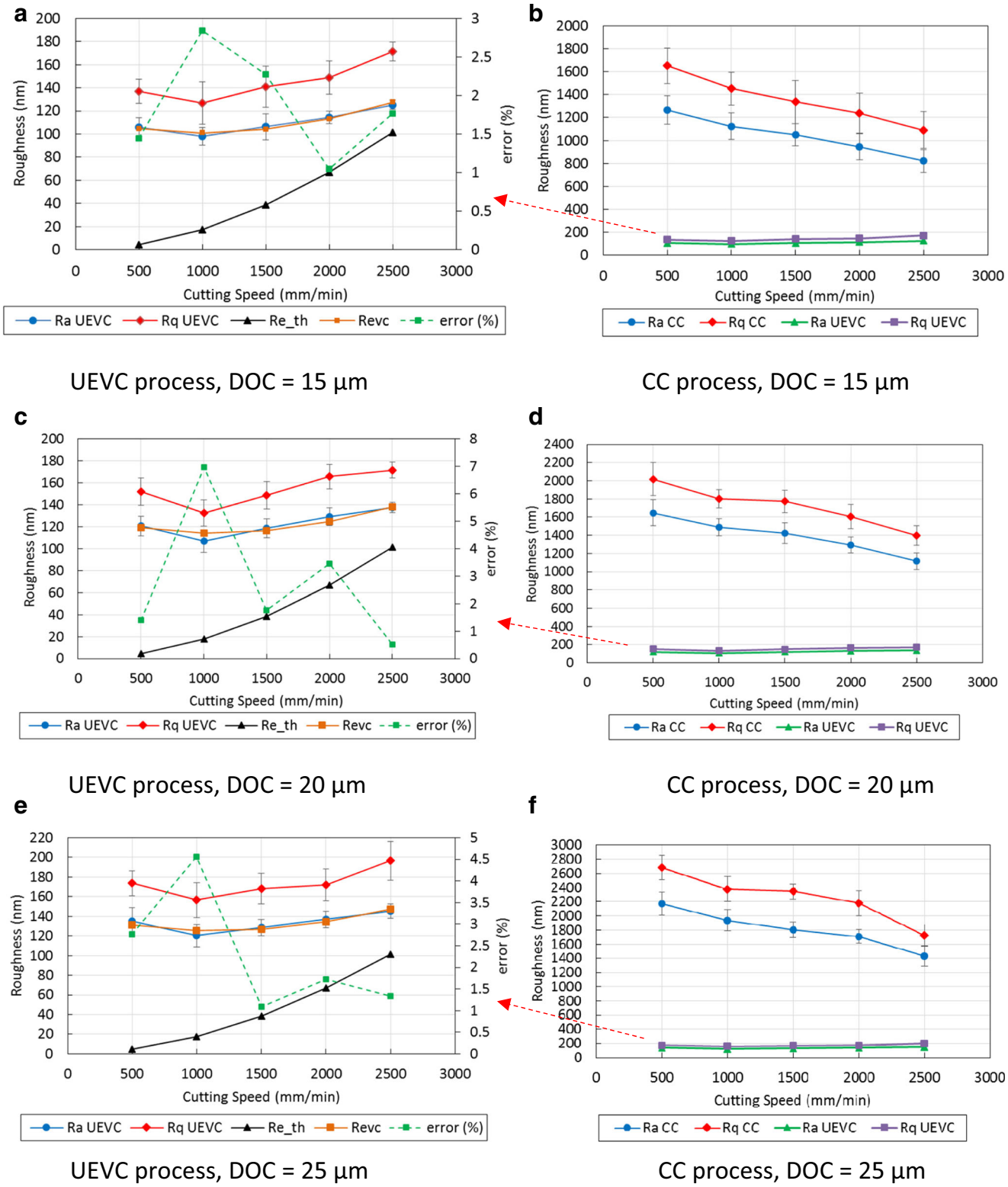

Fig. 14 Surface roughness of microgrooves along cutting speed direction with variation of nominal cutting speeds. UEVC process **a** DOC = 15 µm, **c** DOC = 20 µm, and **e** DOC = 25 µm. CC process **b** DOC = 15 µm, **d** DOC = 20 µm, and **f** DOC = 25 µm

The microgrooves profile along the *x*-direction in the CC case does not have a curvature of the rounded tool nose shape owing to a high cutting resistance, as shown in Fig. 12a. In addition, the side-burr remains high, at approximately 10.14 µm. The side-burr usually occurs owing to the plastic side effect, as hypothesized by Liu et al. [62].

Table 5 Comparison between experimental and model surface roughness

No.	V_F [m/min]	DOC [μm]	f_m [kHz]	φ [°]	R_a [nm] (exp)	R_{e_th} [nm] (theo)	R_{res} [nm] ($R_a - R_{e\_th}$)	R_{res} [nm] (model)	R_{evc} [nm] $R_{e\_th} + R_{res(mod)}$	Error [%]
1.	0.5	15	24	90	106.134	4.5	101.634	100.1	104.6	1.445
2.	0.5	20	24	90	120.503	4.5	116.003	114.325	118.825	1.392
3.	0.5	25	24	90	135.093	4.5	130.593	126.86	131.36	2.763
4.	1.0	15	24	90	98.135	17.6	80.535	83.325	100.925	2.843
5.	1.0	20	24	90	106.811	17.6	89.211	96.64	114.24	6.955
6.	1.0	25	24	90	120.373	17.6	102.773	108.265	125.865	4.562
7.	1.5	15	24	90	106.445	38.6	67.845	65.42	104.02	2.278
8.	1.5	20	24	90	118.521	38.6	79.921	77.825	116.425	1.768
9.	1.5	25	24	90	128.538	38.6	89.938	88.54	127.14	1.087
10.	2.0	15	24	90	114.387	66.8	47.587	46.385	113.185	1.051
11.	2.0	20	24	90	129.143	66.8	62.343	57.88	124.68	3.456
12.	2.0	25	24	90	136.841	66.8	70.041	67.685	134.485	1.722
13.	2.5	15	24	90	125.409	101.4	24.009	26.22	127.62	1.763
14.	2.5	20	24	90	137.51	101.4	36.11	36.805	138.205	0.505
15.	2.5	25	24	90	145.16	101.4	43.786	45.7	147.1	1.334

exp experimental, *theo* theoretical, *res* residual, *mod* model (corresponding to Eq.18)

The work material is under high pressure by the tool edge and then the material flows to the side of the cutting edge creating the side-burr [62]. Meanwhile, the microgroove profile in the UEVC process has an excellent curvature of the rounded tool nose shape, as shown in Fig. 12b. One of the benefits in the UEVC process is that the side burr can be suppressed significantly [39], although the side-burr was not removed completely and still remains at approximately 2.37 μm (Fig. 12b) owing to the effect of the cutting edge radius of the CBN tool ($R_e \geq 3$ μm). The suppressed side-burr effect occurs because the average pushing stress and the average bending stress in the deformation zone on the side edge of burr formation is smaller than that in the CC process [15]. This experimental result indicates that the side-burr is suppressed during R-shape microgrooving by the UEVC process. Similar results of side-burr suppression were obtained by Kim et al. [40] during micro-V grooving using the UEVC process. A reduction in the cutting energy as well as average pushing stress is the one reason that the side-burr can be reduced significantly.

Figure 13 shows the SEM results of the R-shaped microgroove morphology. It can be seen that the CC process at relatively low speeds produces the subsurface fractures in which the surface layers are piled up owing to high cutting resistance, although smooth surfaces are obtained in some regions of the surfaces, as shown in Fig. 13a. In contrast, the UEVC process produces an excellent microgroove morphology and smooth surface roughness. The vibration marks are left after machining, and it is clearly observed at a high magnification of 8000× (Fig. 13b).

5.2 Surface roughness

The surface roughness after microgrooving using both the CC and UEVC processes was evaluated by varying the nominal

Table 6 ANOVA results of R_{res} model corresponding to Eq. 20

Source	DF	Contribution	Seq SS	Adj SS	Adj MS	*F* value	*P* value
R_{res} model	5	98.74%	12,627.9	12,627.9	2525.59	141.61	0.000
V_F	1	88.06%	11,261.7	90.3	90.26	5.06	0.051
DOC	1	10.43%	1333.9	22.4	22.43	1.26	0.291
V_F * V_F	1	0.10%	13.4	13.4	13.35	0.75	0.409
DOC * DOC	1	0.02%	2.4	2.4	2.39	0.13	0.723
V_F * DOC	1	0.13%	16.6	16.6	16.56	0.93	0.360
Residual error	9	1.26%	160.5	160.5	17.83		
Total	14	100%	12,788.4				

Table 7 Validation of surface roughness model

No.	V_F [m/min]	DOC [μm]	f_m [kHz]	φ [°]	R_a [nm] (exp)	R_{e_th} [nm] (theo)	R_{res} [nm] ($R_a - R_{e\_th}$)	R_{res} [nm] (model)	R_{evc} [nm] $R_{e\_th} + R_{res}$ (model)	Error [%]
1	0.5	10	24	90	90.971	4.5	86.471	84.185	88.685	2.513
2	1	10	24	90	80.991	17.6	63.391	68.32	85.92	6.086
3	1.5	10	24	90	94.147	38.6	55.547	51.325	89.925	4.484

cutting speeds (V_F) and increasing the nominal depth of cut (DOC). Figure 14 shows a surface roughness comparison between the CC and UEVC processes. Both arithmetic mean (R_a) and the root mean square (R_q) of the surface roughness are evaluated, as shown in Fig. 14. R_q is always larger than R_a. The surface roughness in the CC process is evidently higher than that in the UEVC process, as shown in Fig. 14. The surface roughness of microgrooves in the CC process decreases with the increase in the nominal cutting speeds from 500 to 2500 mm/min. In general, the surface roughness decreases with increasing cutting speeds [60]. Further, the surface roughness of microgrooves in the UEVC process increases with increasing nominal cutting speed from 1000 to 2500 mm/min. It can be understood that with increasing nominal cutting speed, the elliptical vibration trajectory becomes less overlapped with itself resulting in the increased height of the vibration marks (cusps) [55]. However, the surface roughness becomes high at a low nominal cutting speed of 500 mm/min, which might be due to the effect of elliptical vibration when the elliptical locus overlaps with itself in a small cutting speed ratio [32].

The surface roughness has a stronger tendency to increase when the nominal DOC increases in the case of CC, whereas the surface roughness increases slightly in the case of the UEVC process, as shown in Fig. 14. It can be understood that with increasing nominal DOC, the removed area becomes large leading to an increase the cutting energy as well as the friction load on the rake face; thus, the tool wear mechanism might occur [63] and the rougher surface was obtained for both the CC and UEVC process. Another reason for this could be that with increasing DOC, the stress on the machined surface will increase, resulting in an increase in the number of subsurface fractures or surface cracks at relatively low cutting speeds in the CC process.

Table 5 summarizes the comparison results between the simulated roughness R_{evc} and the experimental roughness R_a, in which the errors are calculated using Eq. 36, where R_a, R_q, R_{e_th}, and R_{evc} are plotted in Fig. 14. As shown in Fig. 14, in the UEVC case (a), (c), and (e), the theoretical surface roughness R_{e_th} decreases sharply when the nominal cutting speeds decreases and it fails to accurately predict the experimental surface roughness value; thus, the residual error surface roughness R_{res} must be added. As we can see in Fig. 14, R_{evc} is able to accurately predict the experimental surface roughness R_a with the error is summarized in Table 5. Table 6 shows the ANOVA results of the residual error roughness R_{res}, in which the greatest contribution factor is influenced by the nominal cutting speed V_F at approximately 88.06% and the DOC is

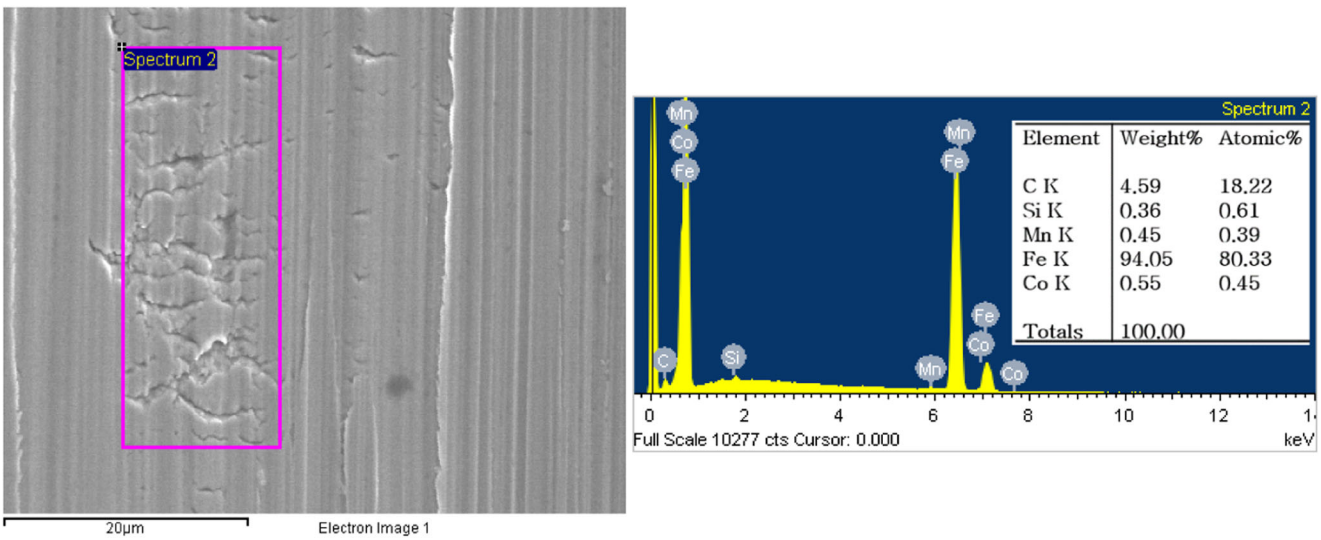

Fig. 15 EDS analysis of microcracks due to the brittle cutting effect in the UEVC process under V_F 1500 mm/min, DOC 25 μm, f_m 24 kHz, and φ 90°

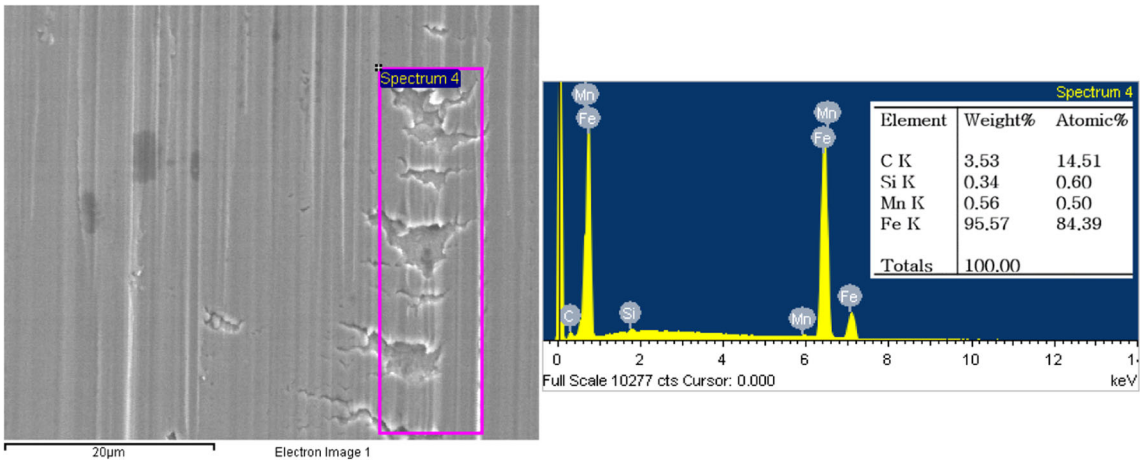

Fig. 16 EDS analysis of microcracks due to the brittle cutting effect in the UEVC process under V_F 2000 mm/min, DOC 25 µm, f_m 24 kHz, and φ 90°

approximately 10.43%. Table 7 shows the validation for the cutting parameters which are different to the cutting parameters which were used in the regression model. The validation confirms that the error is less than 10%.

$$\text{Error}(\%) = \left|\frac{R_a - R_{evc}}{R_a}\right| \times 100\% \tag{36}$$

The microcracks sometimes occur in random locations when the nominal DOC increases during microgrooving using the UEVC process. Microcracks in the UEVC process usually occur under deeper nominal DOC of 25 µm owing to the brittle cutting effect. However, the critical nominal DOC was not investigated in this research when the microcracks starts to generate. In previous contribution by Zhang et al. [35], the microcracks develop when the nominal DOC was increased gradually in the UEVC process. The microcracks occur due to the nature of the AISI 1045 in brittle grain ferrite phase. Because of the nature of the brittle grain, the brittle grains are not tough enough against tensile stress; thus, a massive brittle grains is pulled out from the workpiece when the tool moves the pulling-up motion along the DOC direction [35].

Figures 15 and 16 show the energy-dispersive X-ray analysis to find the atomic composition along boundary of microcrack area. As we can see, there are Si and Mn atoms in the microcrack boundary. These results indicates the presence of Si and Mn in the ferrite (α) grain phase; thus, Si and Mn atoms tend to cause the ferrite (α) grain phase to become more brittle (decreasing the strain to rupture) [60]. The microcrack is unavoidable for large nominal DOC when machining brittle materials using the UEVC process. Nath et al. [64] investigated the critical speed ratio in the UEVC study, and the ductile machining could be obtained by keeping the TOC_t value is smaller than the critical DOC.

5.3 Cutting force

It has been understood that the amount of cutting forces are associated directly with how much the material has been cut. Figure 17b, d, f shows the comparison of cutting forces between the UEVC and CC process for different *DOC* and nominal cutting speeds V_F. The cutting forces in the UEVC process are evidently lower than those in the CC process [43]. The cutting forces typically increase when the DOC increases and the cutting forces slightly increase when the nominal cutting speed V_F increases. The reduction in the cutting forces in the UEVC process is due to the intermittent nature of the UEVC process. In addition, another reason that was suggested was the effect of the friction reversal in the opposite direction to the normal direction while pulling up the deformed chip in elliptical motion and causing the reduced cutting forces [12]. In the other words, the frictional force on the rake face is reversed [12]. Another reason for the reduction in the cutting forces is the effect of increased shear angle during the UEVC process [33]. Because the shear angle increases, the cutting forces significantly decrease. However, the reason for the increased shear angle phenomena in the UEVC still remains scientifically unknown. Zhang et al. [45] proposed the transient shear angle theory during the UEVC process; however, based on experimental results by Kim et al. [33], the shear angle seems to have a constant value above approximately 30°.

Figure 17a, c, e shows comparison cutting forces in the UEVC process between experimental and predicted cutting forces. The F_{cp} cutting force represents the value of the principle cutting force in nominal cutting speed V_F or *y*-axis direction. The F_{ct} cutting force represents the value of the thrust cutting force in the normal direction or *z*-axis direction. As we can see in Fig. 17, the predicted cutting forces in the UEVC are similar with the experimental data. As shown in Fig. 17, the percentage error of the

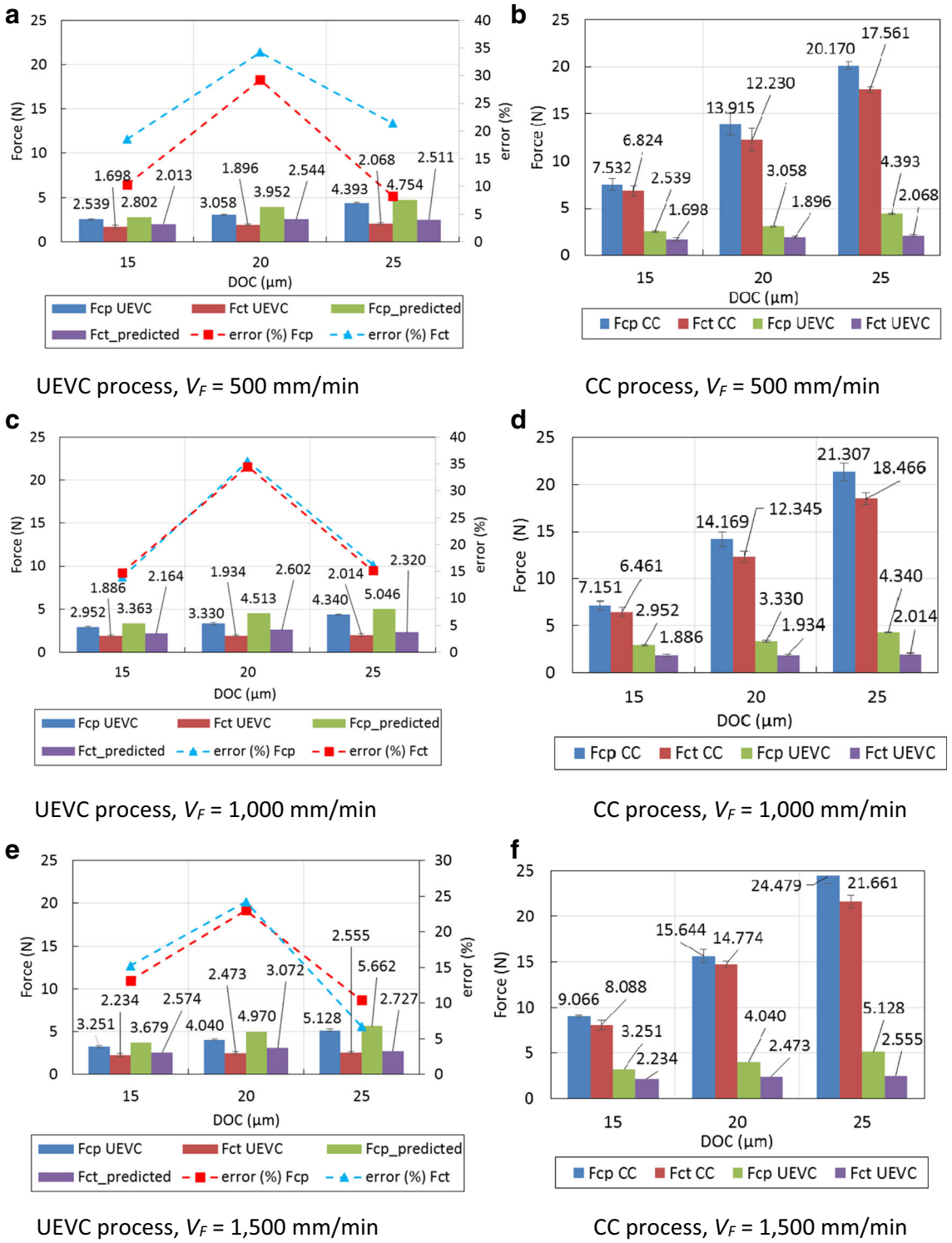

Fig. 17 Cutting force comparison between the UEVC and CC microgrooving process with various cutting speeds

cutting forces between experimental and simulation is calculated using Eq. 37.

$$\text{Error}(\%) = \left| \frac{F_{\text{experiment}} - F_{\text{predicted}}}{F_{\text{experiment}}} \right| \times 100\% \tag{37}$$

where the predicted cutting forces both the principle and thrust are described using Eqs. 34 and 35, respectively.

In order to find the predicted cutting forces, the specific cutting force constant of principle K_{fp} and thrust K_{ft} can be found by dividing cutting force F_{cp} and F_{ct} experimental with A_{cut_rms}.

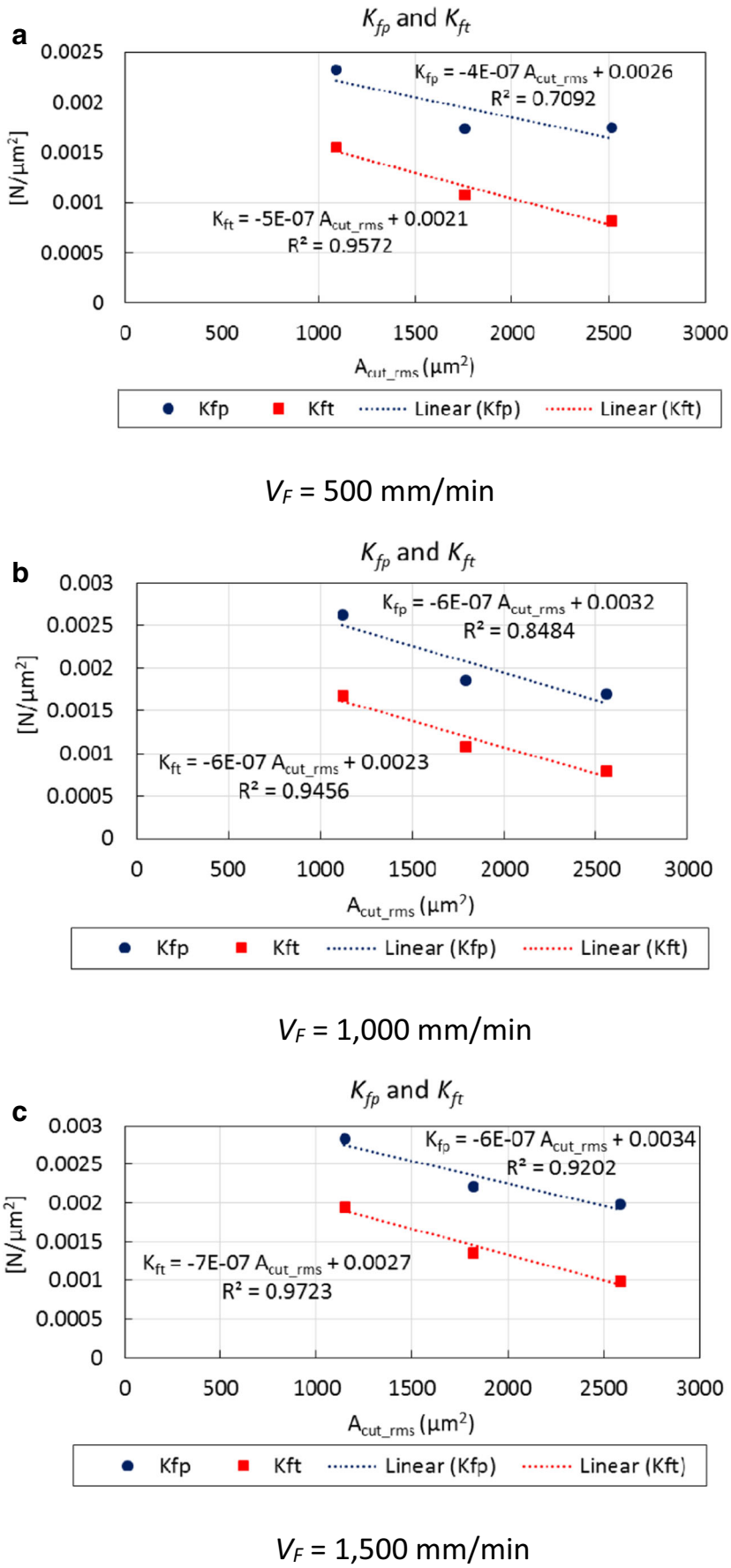

Fig. 18 Cutting force coefficient constant in the UEVC process with different A_{cut_rms} at **a** V_F = 500 mm/min, **b** V_F = 1000 mm/min, and **c** V_F = 1500 mm/min, f_m = 24 kHz, and φ = 90°

Table 8 Validation of cutting force model

No	V_F [m/min]	DOC [μm]	f_m [kHz]	φ [°]	A_{cut_rms} [μm^2]	K_{fp} [N/μm^2]	K_{ft} [N/μm^2]	F_{CPrms} [N]	F_{CTrms} [N]	$F_{CP(exp)}$ [N]	$F_{CT(exp)}$ [N]	Error (%) [F_{CP}]	Error (%) [F_{CT}]
1	0.5	10	24	90	542.92	0.002383	0.001829	1.534	1.177	1.977	0.935	22.43	25.88
2	1	10	24	90	570.63	0.002858	0.001958	1.927	1.319	2.274	1.059	15.28	24.60
3	1.5	10	24	90	590.80	0.003046	0.002286	2.119	1.590	2.532	1.249	16.31	27.27

$$K_{fp} = \frac{F_{CP}(experimental)}{A_{cut\_rms}} \left[N/\mu m^2\right] \tag{38}$$

$$K_{ft} = \frac{F_{CT}(experimental)}{A_{cut\_rms}} \left[N/\mu m^2\right] \tag{39}$$

where A_{cut_rms} (Eq. 41) is the cutting area on the rake face when the root mean square of transient thickness of cut TOC_{t_rms} is considered, where n is number of data used during the numerical calculation from time t_A to t_D.

$$TOC_{t\_rms} = \sqrt{\frac{1}{n}\sum_{i=1}^{i=n}[TOC_t(t_i)]^2}\ 1 \le i \le n \tag{40}$$

$$A_{cut\_rms} = \left\{R^2 \cdot cos^{-1}\left(\frac{R - TOC_{t\_rms}}{R}\right)\right\} - \left\{(R - TOC_{t\_rms})\sqrt{2 \cdot R \cdot TOC_{t\_rms} - TOC_{t\_rms}{}^2}\right\} \tag{41}$$

The value of K_{fp} and K_{ft} is related directly to the machining parameters. As shown in Fig. 18, the cutting force coefficients are determined by curve fitting in linear way as a function of

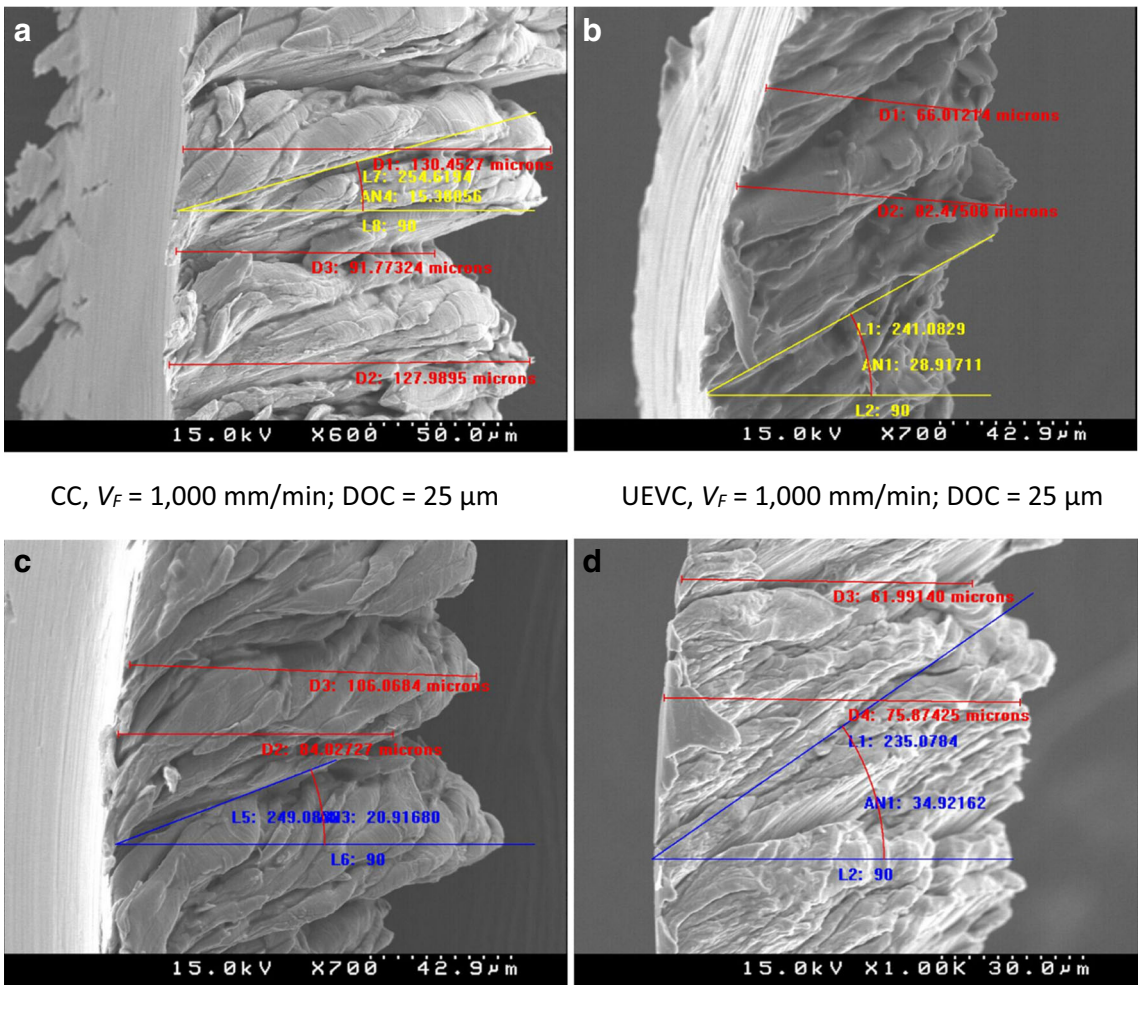

CC, V_F = 1,000 mm/min; DOC = 25 μm

UEVC, V_F = 1,000 mm/min; DOC = 25 μm

CC, V_F = 1,500 mm/min; DOC = 25 μm

UEVC, V_F = 1,500 mm/min; DOC = 25 μm

Fig. 19 Shear angle and chip thickness between the CC and the UEVC process in AISI 1045

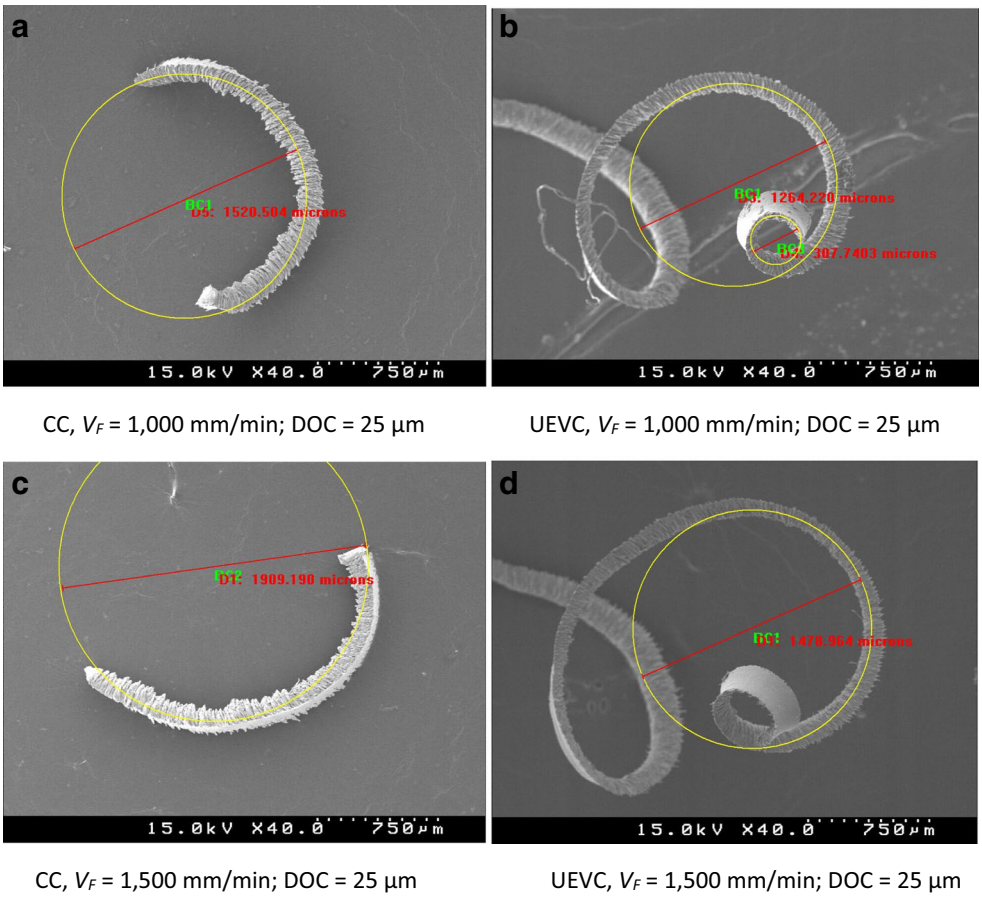

CC, V_F = 1,000 mm/min; DOC = 25 µm

UEVC, V_F = 1,000 mm/min; DOC = 25 µm

CC, V_F = 1,500 mm/min; DOC = 25 µm

UEVC, V_F = 1,500 mm/min; DOC = 25 µm

Fig. 20 Curvature radius of the chip formation between the CC and the UEVC processes in AISI 1045

A_{cut_rms}. The cutting force model is validated as shown in Table 8, where the cutting parameters are different to the cutting parameters which were used in the regression model. The validation confirms that the error between the predicted cutting force (rms) and the experimental cutting force is lower than 30%.

5.4 Chip formation

In this section, the chip formation both using CC and UEVC process are compared after conducting the microgrooving experiments. The shear angle, chip thickness, and chip curvature radius were investigated for both methods. The shear angle and chip thickness are presented in Fig. 19, which shows the SEM images for both methods with different nominal cutting speeds with constant DOC of 25 µm. The UEVC process evidently produces a higher shear angle value with a thinner chip thickness than that in the CC process and it becomes one of the reasons that the cutting forces decrease. Because the shear angle increases in the UEVC process, the chip thickness reduces accordingly [33]. In case of nominal cutting speed V_F = 1000 mm/min in UEVC, a lower shear angle of approximately 28.917° was obtained, whereas for a higher nominal cutting speed of

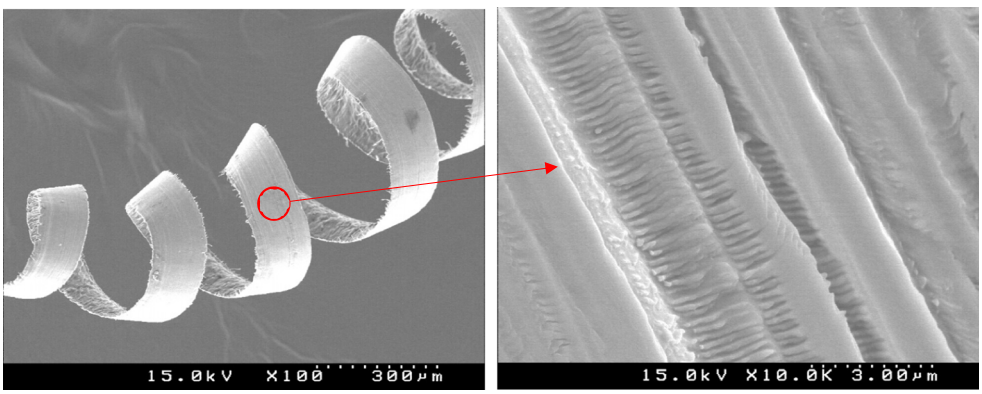

Fig. 21 Continuous, thin, and spiral chip formation and vibration marks produced on the rake–chip contact surface in UEVC microgrooving with V_F = 1000 mm/min; DOC = 15 µm, f_m = 24 kHz, and φ = 90°

1500 mm/min in UEVC, a higher shear angle of approximately 34.92° was obtained. In the case of nominal cutting speed V_F = 1000 and 1500 mm/min in CC, the shear angle is approximately 15.80° and 20.91°, respectively. These experimental results indicate that by increasing the nominal cutting speeds, the shear angle value increases. The reasons for this effect of increased shear angle in the UEVC process remains unknown. However, scientists argued that this was due to the effect of the friction reversal in the elliptical vibration nature [12, 33]. These high shear angle values in the UEVC process provides a sustainable steel cutting in the microgrooving process in relatively low nominal cutting speeds.

Both the CC and UEVC processes produce continuous chips. However, in case of UEVC, spiral, thin, and continuous chips are produced. A comparison of the curvature radius between the CC and UEVC processes is shown in Fig. 20. The curvature radius of chip formation in the UEVC is evidently smaller than that in the CC process. These experimental results are similar to those of Kim et al. [39], where the chip curvature in the UEVC is relatively small. In case of the CC process, a relatively large shear deformation with large cutting resistance occurs on the shear stress plane, in which the continuous chips with large curvature radius as well as large chip thickness and low shear angle are generated. However, in the UEVC process, a relatively low shear deformation and low cutting resistance on the shear stress plane owing to intermittent behavior establishes the continuous chips with large shear angle, small curvature radius, and relatively thin chip thickness. Figure 21 shows the continuous, spiral, thin, and small curvature radius with a vibration marks that were observed clearly on the chip–rake contact surface using the UEVC process.

6 Conclusions

An experimental and analytical study using the CC and UEVC processes in microgrooving have been carried out, and the conclusions are summarized as follows:

- It is experimentally proved that the UEVC process during microgrooving has better performances such as reduced surface roughness, decreased cutting force, reduced sideburr, better microgroove profile, and better chip formation compared to the CC method. These results indicate the achievement of sustainable machining during microgrooving manufacturing.
- The theoretical surface roughness in the UEVC process fails to accurately predict, and thus the residual error should be added in the model to predict accurately. The surface roughness in the UEVC process increases gradually when the nominal cutting speeds increase; however, the surface roughness in the CC process decreases gradually when the nominal cutting speeds increase.
- The brittle fracture occurs even in the UEVC process if the nominal DOC increases beyond approximately 25 μm. Microcracks occur owing to the nature of the AISI 1045 in the brittle ferrite phase.
- The UEVC process generates low cutting forces during microgrooving. In addition, a cutting force model for the UEVC process has been proposed and validated in this research. By obtaining the value of the cutting coefficient for both principle K_{fp} and thrust K_{ft}, the cutting force model can accurately predict by calculating transient TOC as well as the transient cutting area.
- The UEVC process produces a chip formation that typically has a continuous, spiral shape, large shear angle, thin chip thickness, and small curvature radius. This indicates a relatively low shear deformation and low cutting resistance on the shear stress plane owing to intermittent cutting behavior in the UEVC process.

Acknowledgements This research was supported by Basic Science Research Program through the National Research Foundation of Korea (NRF) funded by the Ministry of Science, ICT and Future Planning (grant number NRF-2017R1A2B2003932). Also, this work was supported by the 2017 Yeungnam University Research Grant. This work has been also supported by the Basic Science Research Program through the National Research Foundation of Korea (NRF) funded by the Ministry of Education (NRF-2017R1A4A1015581).

Nomenclature $y(t)$, relative tool tip position of UEVC method along y-axis without considering effect of edge radius; $z(t)$, relative tool tip position of UEVC method along z-axis without considering effect of edge radius; $y_e(t)$, relative tool tip position of point CC' along y-axis; $z_e(t)$, relative tool tip position of point CC' along z-axis; $V_y(t)$, tool tip velocity of UEVC method along y-axis; $V_z(t)$, tool tip velocity of UEVC method along z-axis; $\overrightarrow{V_t}(t)$, transient velocity vector; $|V_t(t)|$, magnitude velocity vector; $\theta(t)$, slope angle of the elliptical path; a, elliptical locus minor amplitude along y-axis; b, elliptical locus major amplitude along z-axis; f_m, ultrasonic vibration frequency; φ, phase shift; V_F, nominal cutting speed; t, time; R, tool nose radius; R_e, tool cutting edge radius; F, cross feed distance; db, width of microgrooves shape; Lb, gap between two neighboring grooves; R_{evc}, surface roughness model in UEVC process; R_{e_th}, theoretical surface roughness considering tool edge radius; R_{res}, residual error surface roughness; t_A, time when cutting tool leaves in the profile in one cycle time period; t_A', time when cutting tool comes in the profile in one cycle time period; $F_{CP}(t)$, principle cutting force; $F_{CT}(t)$, thrust cutting force; $K_{fp}(t)$, cutting force coefficient for principle cutting force; $K_{ft}(t)$, cutting force coefficient for thrust cutting force; $A_{cut}(t)$, transient cutting area; $TOC_t(t)$, transient thickness of cut; DOC, nominal depth of cut

References

1. Gachot C, Rosenkranz A, Hsu SM, Costa HL (2017) A critical assessment of surface texturing for friction and wear improvement. Wear 372–373:21–41. https://doi.org/10.1016/j.wear.2016.11.020

2. Yuan S, Huang W, Wang X (2011) Orientation effects of micro-grooves on sliding surfaces. Tribol Int 44:1047–1054. https://doi.org/10.1016/j.triboint.2011.04.007
3. Kurniawan R, Ko TJ (2015) Friction reduction on cylindrical surfaces by texturing with a piezoelectric actuated tool holder. Int J Precis Eng Manuf 16:861–868. https://doi.org/10.1007/s12541-015-0113-2
4. Wakuda M, Yamauchi Y, Kanzaki S, Yasuda Y (2003) Effect of surface texturing on friction reduction between ceramic and steel materials under lubricated sliding contact. Wear 254:356–363. https://doi.org/10.1016/S0043-1648(03)00004-8
5. Etsion I (2013) Modeling of surface texturing in hydrodynamic lubrication. Friction 1:195–209. https://doi.org/10.1007/s40544-013-0018-y
6. Sharma V, Pandey PM (2016) Recent advances in turning with textured cutting tools: a review. J Clean Prod 137:701–715. https://doi.org/10.1016/j.jclepro.2016.07.138
7. Arslan A, Masjuki HH, Kalam MA, Varman M, Mufti RA, Mosarof MH, Khuong LS, Quazi MM (2016) Surface texture manufacturing techniques and tribological effect of surface texturing on cutting tool performance: a review. Crit Rev Solid State Mater Sci 8436: 1–35. https://doi.org/10.1080/10408436.2016.1186597
8. Chetan GS, Venkateswara Rao P (2015) Application of sustainable techniques in metal cutting for enhanced machinability: a review. J Clean Prod 100:17–34. https://doi.org/10.1016/j.jclepro.2015.03.039
9. Kawasegi N, Sugimori H, Morimoto H, Morita N, Hori I (2009) Development of cutting tools with microscale and nanoscale textures to improve frictional behavior. Precis Eng 33:248–254. https://doi.org/10.1016/j.precisioneng.2008.07.005
10. Sugihara T, Enomoto T (2009) Development of a cutting tool with a nano/micro-textured surface—improvement of anti-adhesive effect by considering the texture patterns. Precis Eng 33:425–429. https://doi.org/10.1016/j.precisioneng.2008.11.004
11. Xie J, Luo MJ, Wu KK, Yang LF, Li DH (2013) Experimental study on cutting temperature and cutting force in dry turning of titanium alloy using a non-coated micro-grooved tool. Int J Mach Tools Manuf 73:25–36. https://doi.org/10.1016/j.ijmachtools.2013.05.006
12. Shamoto E, Moriwaki T (1994) Study on elliptical vibration cutting. CIRP Ann Manuf Technol 43:35–38. https://doi.org/10.1016/S0007-8506(07)62158-1
13. Kim GD, Loh BG (2007) An ultrasonic elliptical vibration cutting device for micro V-groove machining: kinematical analysis and micro V-groove machining characteristics. J Mater Process Technol 190:181–188. https://doi.org/10.1016/j.jmatprotec.2007.02.047
14. Saito H, Jung H, Shamoto E, Wu TC, Chien JT (2017) Mirror surface machining of high-alloy steels by elliptical vibration cutting with single-crystalline diamond tools: influence of alloy elements on diamond tool damage. Precis Eng 49:200–210. https://doi.org/10.1016/j.precisioneng.2017.02.008
15. Ma C, Shamoto E, Moriwaki T, Zhang Y, Wang L (2005) Suppression of burrs in turning with ultrasonic elliptical vibration cutting. Int J Mach Tools Manuf 45:1295–1300. https://doi.org/10.1016/j.ijmachtools.2005.01.011
16. Shamoto E, Moriwaki T (1999) Ultaprecision diamond cutting of hardened steel by applying elliptical vibration cutting. CIRP Ann Manuf Technol 48:441–444 https://doi.org/10.1016/S0007-8506(07)63222-3
17. Nath C, Rahman M, Neo KS (2009) Machinability study of tungsten carbide using PCD tools under ultrasonic elliptical vibration cutting. Int J Mach Tools Manuf 49:1089–1095. https://doi.org/10.1016/j.ijmachtools.2009.07.006
18. Nath C, Rahman M, Neo KS (2009) A study on ultrasonic elliptical vibration cutting of tungsten carbide. J Mater Process Technol 209: 4459–4464. https://doi.org/10.1016/j.jmatprotec.2008.10.047
19. Zhang X, Senthil Kumar A, Rahman M et al (2011) Experimental study on ultrasonic elliptical vibration cutting of hardened steel using PCD tools. J Mater Process Technol 211:1701–1709. https://doi.org/10.1016/j.jmatprotec.2011.05.015
20. Suzuki N, Masuda S, Haritani M, Shamoto E (2004) Ultraprecision micromachining of brittle materials by applying ultrasonic elliptical vibration cutting. In: Micro-Nanomechatronics and Human Science, 2004 and The Fourth Symposium Micro-Nanomechatronics for Information-Based Society, 2004. Ieee, pp 133–138
21. Bai W, Sun R, Gao Y, Leopold J (2016) Analysis and modeling of force in orthogonal elliptical vibration cutting. Int J Adv Manuf Technol 83:1025–1036. https://doi.org/10.1007/s00170-015-7645-6
22. Geng D, Zhang D, Li Z, Liu D (2017) Feasibility study of ultrasonic elliptical vibration-assisted reaming of carbon fiber reinforced plastics/titanium alloy stacks. Ultrasonics 75:80–90. https://doi.org/10.1016/j.ultras.2016.11.011
23. Chen JB, Fang QH, Wang CC, Du JK, Liu F (2016) Theoretical study on brittle-ductile transition behavior in elliptical ultrasonic assisted grinding of hard brittle materials. Precis Eng 46:104–117. https://doi.org/10.1016/j.precisioneng.2016.04.005
24. Liu D, Yan R, Chen T (2017) Material removal model of ultrasonic elliptical vibration-assisted chemical mechanical polishing for hard and brittle materials. Int J Adv Manuf Technol 92:81–99. https://doi.org/10.1007/s00170-017-0081-z
25. Huang W, Yu D, Zhang M, Ye F, Yao J (2017) Analytical design method of a device for ultrasonic elliptical vibration cutting. J Acoust Soc Am 141:1238–1245. https://doi.org/10.1121/1.4976340
26. Jung H, Hayasaka T, Shamoto E (2016) Mechanism and suppression of frictional chatter in high-efficiency elliptical vibration cutting. CIRP Ann Manuf Technol 65:369–372. https://doi.org/10.1016/j.cirp.2016.04.103
27. Lotfi M, Amini S (2017) FE simulation of linear and elliptical ultrasonic vibrations in turning of Inconel 718. Proc Inst Mech Eng Part E J Process Mech Eng. https://doi.org/10.1177/0954408917715533
28. Zhang J, Suzuki N, Wang Y, Shamoto E (2015) Ultra-precision nano-structure fabrication by amplitude control sculpturing method in elliptical vibration cutting. Precis Eng 39:86–99. https://doi.org/10.1016/j.precisioneng.2014.07.009
29. Zhang J, Cui T, Ge C, Sui Y, Yang H (2016) Review of micro/nano machining by utilizing elliptical vibration cutting. Int J Mach Tools Manuf 106:109–126. https://doi.org/10.1016/j.ijmachtools.2016.04.008
30. Yang Y, Pan Y, Guo P (2017) Structural coloration of metallic surfaces with micro/nano-structures induced by elliptical vibration texturing. Appl Surf Sci 402:400–409. https://doi.org/10.1016/j.apsusc.2017.01.026
31. Kurniawan R, Kiswanto G, Ko TJ (2016) Micro-dimple pattern process and orthogonal cutting force analysis of elliptical vibration texturing. Int J Mach Tools Manuf 106:127–140. https://doi.org/10.1016/j.ijmachtools.2016.03.007
32. Kurniawan R, Kiswanto G, Ko TJ (2017) Surface roughness of two-frequency elliptical vibration texturing (TFEVT) method for micro-dimple pattern process. Int J Mach Tools Manuf 116:77–95. https://doi.org/10.1016/j.ijmachtools.2016.12.011
33. Kim GD, Loh BG (2007) Characteristics of chip formation in micro V-grooving using elliptical vibration cutting. J Micromech Microeng 17:1458–1466. https://doi.org/10.1088/0960-1317/17/8/007

34. Xu W, Zhang LC, Wu Y (2014) Elliptic vibration-assisted cutting of fibre-reinforced polymer composites: understanding the material removal mechanisms. Compos Sci Technol 92:103–111. https://doi.org/10.1016/j.compscitech.2013.12.011
35. Zhang J, Suzuki N, Wang Y, Shamoto E (2014) Fundamental investigation of ultra-precision ductile machining of tungsten carbide by applying elliptical vibration cutting with single crystal diamond. J Mater Process Technol 214:2644–2659. https://doi.org/10.1016/j.jmatprotec.2014.05.024
36. Suzuki H, Hamada S, Okino T, Kondo M, Yamagata Y, Higuchi T (2010) Ultraprecision finishing of micro-aspheric surface by ultrasonic two-axis vibration assisted polishing. CIRP Ann Manuf Technol 59:347–350. https://doi.org/10.1016/j.cirp.2010.03.117
37. Ma C, Ma J, Shamoto E, Moriwaki T (2011) Analysis of regenerative chatter suppression with adding the ultrasonic elliptical vibration on the cutting tool. Precis Eng 35:329–338. https://doi.org/10.1016/j.precisioneng.2010.12.004
38. Kim GD, Loh BG (2011) Direct machining of micro patterns on nickel alloy and mold steel by vibration assisted cutting. Int J Precis Eng Manuf 12:583–588. https://doi.org/10.1007/s12541-011-0075-y
39. Kim GD, Loh BG (2010) Machining of micro-channels and pyramid patterns using elliptical vibration cutting. Int J Adv Manuf Technol 49:961–968. https://doi.org/10.1007/s00170-009-2451-7
40. Kim GD, Loh BG (2008) Characteristics of elliptical vibration cutting in micro-V grooving with variations in the elliptical cutting locus and excitation frequency. J Micromech Microeng 18:025002. https://doi.org/10.1088/0960-1317/18/2/025002
41. Zhang C, Ehmann K, Li Y (2015) Analysis of cutting forces in the ultrasonic elliptical vibration-assisted micro-groove turning process. Int J Adv Manuf Technol 78:139–152. https://doi.org/10.1007/s00170-014-6628-3
42. Guo P, Lu Y, Pei P, Ehmann KF (2014) Fast generation of microchannels on cylindrical surfaces by elliptical vibration texturing. J Manuf Sci Eng 136:041008. https://doi.org/10.1115/1.4027126
43. Ma C, Shamoto E, Moriwaki T, Wang L (2004) Study of machining accuracy in ultrasonic elliptical vibration cutting. Int J Mach Tools Manuf 44:1305–1310. https://doi.org/10.1016/j.ijmachtools.2004.04.014
44. Shamoto E, Suzuki N, Hino R (2008) Analysis of 3D elliptical vibration cutting with thin shear plane model. CIRP Ann Manuf Technol 57:57–60. https://doi.org/10.1016/j.cirp.2008.03.073
45. Zhang X, Senthil Kumar A, Rahman M et al (2012) An analytical force model for orthogonal elliptical vibration cutting technique. J Manuf Process 14:378–387. https://doi.org/10.1016/j.jmapro.2012.05.006
46. Jieqiong L, Jinguo H, Xiaoqin Z, Zhaopeng H, Mingming L (2016) Study on predictive model of cutting force and geometry parameters for oblique elliptical vibration cutting. Int J Mech Sci 117:43–52. https://doi.org/10.1016/j.ijmecsci.2016.08.004
47. Wen JODO, Apa JOCP, Eimers JAR et al (2017) Design , fabrication , and testing of convex reflective diffraction gratings. Opt Express 25:808–816
48. Zhang Y, Wang S, Ding P (2017) Effects of channel shape on the cooling performance of hybrid micro-channel and slot-jet module. Int J Heat Mass Transf 113:295–309. https://doi.org/10.1016/j.ijheatmasstransfer.2017.05.092
49. Takeuchi Y, Maeda S, Kawai T, Sawada K (2002) Manufacture of multiple focus micro fresnel lenses by means of nonrotational diamond grooving. CIRP Ann Manuf Technol 51:5–8
50. Sawada K, Kawai T, Takeuchi Y, Sata T (2000) Development of ultraprecisison micro grooving (manufacture of V-shaped groove). JSME Int J 43:170–176
51. Song KY, Chung DK, Soo M et al (2013) Fabrication of microlenticular patterns using WEDM-grooving and electrolytic polishing. J Micromech Microeng 23:11. https://doi.org/10.1088/0960-1317/23/12/125034
52. Yan J, Kaneko T, Uchida K (2010) Fabricating microgrooves with varied cross-sections by electrodischarge machining. 991–1002. doi: https://doi.org/10.1007/s00170-010-2563-0
53. Kiswanto G, Zariatin DL, Ko TJ (2014) The effect of spindle speed , feed-rate and machining time to the surface roughness and burr formation of Aluminum Alloy 1100 in micro-milling operation. 16:435–450 . doi: https://doi.org/10.1016/j.jmapro.2014.05.003
54. Guo P, Ehmann KF (2013) Development of a tertiary motion generator for elliptical vibration texturing. Precis Eng 37:364–371. https://doi.org/10.1016/j.precisioneng.2012.10.005
55. Zhang X, Kumar a S, Rahman M, Liu K (2013) Modeling of the effect of tool edge radius on surface generation in elliptical vibration cutting. Int J Adv Manuf Technol 65:35–42. https://doi.org/10.1007/s00170-012-4146-8
56. Merchant ME (1945) Mechanics of the metal cutting process. I. Orthogonal cutting and a type 2 Chip. J Appl Phys 16:267–275. https://doi.org/10.1063/1.1707586
57. Altintas Y (2012) Manufacturing automation-metal cutting mechanics, machine tool vibrations, and CNC design, 2nd edn. Cambridge University Press, United States
58. Zhu W, He Y, Ehmann KF, et al (2017) Modeling of the effects of phase shift on cutting performance in elliptical vibration cutting Modeling of the effects of phase shift on cutting performance in elliptical vibration cutting. doi: https://doi.org/10.1007/s00170-017-0366-2
59. Freitas VL de A, de AVHC, Silva E de M et al (2010) Nondestructive characterization of microstructures and determination of elastic properties in plain carbon steel using ultrasonic measurements. Mater Sci Eng A 527:4431–4437. https://doi.org/10.1016/j.msea.2010.03.090
60. Shaw M (1984) Metal cutting principles, 1st edition, Oxford University Press, United States, 1984.
61. Kurniawan R, Ko TJ, Ping LC, Kumaran ST, Kiswanto G, Guo P, Ehmann KF (2017) Development of a two-frequency, elliptical-vibration texturing device for surface texturing. J Mech Sci Technol 31:3465–3473. https://doi.org/10.1007/s12206-017-0635-x
62. Liu K, Melkote SN (2006) Effect of plastic side flow on surface roughness in micro-turning process. Int J Mach Tools Manuf 46:1778–1785. https://doi.org/10.1016/j.ijmachtools.2005.11.014
63. Özel T, Hsu TK, Zeren E (2005) Effects of cutting edge geometry, workpiece hardness, feed rate and cutting speed on surface roughness and forces in finish turning of hardened AISI H13 steel. Int J Adv Manuf Technol 25:262–269. https://doi.org/10.1007/s00170-003-1878-5
64. Nath C, Rahman M, Neo KS (2011) Modeling of the effect of machining parameters on maximum thickness of cut in ultrasonic elliptical vibration cutting. J Manuf Sci Eng 133:011007. https://doi.org/10.1115/1.4003118